J. Fluid Mech. (2008), *vol.* 604, *pp.* 125–163. © 2008 Cambridge University Press
doi:10.1017/S0022112008001079 Printed in the United Kingdom

New dynamic subgrid-scale heat flux models for large-eddy simulation of thermal convection based on the general gradient diffusion hypothesis

BING-CHEN WANG[1], EUGENE YEE[1],
DONALD J. BERGSTROM[2] AND OAKI IIDA[3]

[1]Defence Research & Development Canada – Suffield,
P.O. Box 4000, Medicine Hat, AB, T1A 8K6, Canada
bingchen.wang@drdc-rddc.gc.ca, eugene.yee@drdc-rddc.gc.ca

[2]Department of Mechanical Engineering, University of Saskatchewan,
57 Campus Drive, Saskatoon, S7N 5A9, SK, Canada
don.bergstrom@usask.ca

[3]Department of Mechanical Engineering, Nagoya Institute of Technology,
Gokiso-cho, Showa-ku, Nagoya 466-8555, Japan
iida.oaki@nitech.ac.jp

(Received 18 December 2006 and in revised from 13 February 2008)

Three new dynamic tensor thermal diffusivity subgrid-scale (SGS) heat flux (HF) models are proposed for large-eddy simulation of thermal convection. The constitutive relations for the proposed modelling approaches represent the most general explicit algebraic formulations possible for the family of SGS HF models constructed using the resolved temperature gradient and SGS stress tensor. As a result, these three new models include a number of previously proposed dynamic SGS HF models as special cases. In contrast to the classical dynamic eddy thermal diffusivity SGS HF model, which strictly requires the SGS heat flux be aligned with the negative of the resolved temperature gradient, the three new models proposed here admit more degrees of freedom, and consequently provide a more realistic geometrical and physical representation of the SGS HF vector. To validate the proposed models, numerical simulations have been performed based on two benchmark test cases of neutrally and unstably stratified horizontal channel flows.

1. Introduction

The application of a dynamic procedure to subgrid-scale (SGS) heat flux (HF) modelling was introduced for large-eddy simulation (LES) of scalar transport shortly after the dynamic SGS stress model was proposed by Germano *et al.* (1991). Moin *et al.* (1991) proposed a dynamic linear eddy thermal diffusivity model (EDM) for representing the SGS heat flux. The EDM is based on a linear constitutive relation analogous to Fourier's law for describing molecular heat conduction, and assumes that the SGS HF vector is instantaneously proportional to and aligned with the negative of the resolved temperature gradient, i.e. $h_j \propto -\partial\bar{\theta}/\partial x_j$. It is known that this overly simplified linear constitutive relation is inconsistent with the physics of turbulent convection (Salvetti & Banerjee 1995; Peng & Davidson 2002; Porté-Agel *et al.* 2001*a,b*; Higgins, Parlange & Meneveau 2004; Wang *et al.* 2007*a,b*) and does not correctly reflect the local geometrical property of the SGS HF vector. In spite of these deficiencies, the EDM is still the most popular SGS HF model and has been applied to predictions of various thermal convective flows with some success (see Lee, Xu & Pletcher 2004; Pallares & Davidson 2002; Avancha & Pletcher 2002; Dailey, Meng & Petcher 2003; Keating *et al.* 2004; Wang & Lu 2004; Tyagi & Acharya 2005; Garg *et al.* 2000; Armenio & Sarkar 2002).

During the past decade, dynamic SGS HF models progressed from models of the eddy thermal diffusivity (or more briefly, eddy diffusivity, represented by α_{sgs}) type to those based on a tensor thermal diffusivity (or more briefly, tensor diffusivity, represented by D_{ij}) in order to further improve the physical and geometrical representation of the SGS HF vector. Based on the original concept of scale-similarity for modelling the SGS stress of Bardina, Ferziger & Reynolds (1980), Salvetti & Banerjee (1995) introduced a dynamic scale-similarity SGS HF model. Salvetti & Banerjee (1995) also introduced a dynamic two-parameter mixed model (DMM) for representing the SGS heat flux, which combines the linear eddy diffusivity SGS HF model with a scale-similarity SGS HF model. By using truncated Taylor series expansions for approximating filtered flow variables, Porté-Agel *et al.* (2001*a,b*) and Kang & Meneveau (2002) developed a simplified DMM (SDMM), which combines the dynamic linear eddy diffusivity SGS HF model with a dynamic gradient SGS HF model (DGM). The DGM in the approach of Porté-Agel *et al.* (2001*a,b*) and Kang & Meneveau (2002) is analogous to Clark's model for modelling the SGS stress (Clark, Ferziger & Reynolds 1979), and uses the resolved velocity gradient tensor ($\bar{A}_{ij} \overset{\text{def}}{=} \partial \bar{u}_i / \partial x_j$) to build the tensor thermal diffusivity (i.e. $D_{jk} \propto \bar{A}_{jk}$, see also figure 1). This SDMM has been applied to the investigation of heat fluxes and dissipation in an atmospheric boundary layer flow and in a heated wind-tunnel wake flow using the *a priori* LES approach (Porté-Agel *et al.* 2001*a,b*; Kang & Meneveau 2002; Higgins *et al.* 2004). In contrast to the approach of dynamic mixed SGS HF models, Peng & Davidson (2002) proposed a dynamic homogeneous linear tensor diffusivity model (DHLTDM) for representing the SGS heat flux in their study of a buoyancy-driven turbulent flow. In their approach, the tensor diffusivity is constructed as a homogeneous linear function of the resolved strain rate tensor (defined as $\bar{S}_{ij} \overset{\text{def}}{=} (\partial \bar{u}_i / \partial x_j + \partial \bar{u}_j / \partial x_i)/2$). Using the theory of tensor functions, Wang *et al.* (2007*a,b*) recently proposed a dynamic inhomogeneous linear tensor diffusivity model (DILTDM), a dynamic full linear tensor diffusivity model (DFLTDM) and a dynamic nonlinear tensor diffusivity model (DNTDM) for representation of the SGS HF. The tensor diffusivity for the DILTDM is constructed as an inhomogeneous linear function of the resolved strain rate and rotation rate tensors (the latter is defined as $\bar{\Omega}_{ij} \overset{\text{def}}{=} (\partial \bar{u}_i / \partial x_j - \partial \bar{u}_j / \partial x_i)/2$) (Wang *et al.* 2007*a*); whereas, the tensor diffusivities for the DFLTDM and DNTDM are constructed as a full linear and a quadratic nonlinear function of the strain rate tensor (Wang *et al.* 2007*b*), respectively. The DILTDM, DFLTDM and DNTDM have been tested using a canonical mixed forced and natural convective flow confined in a vertical channel. The SGS HF models mentioned above are identified as dynamic explicit algebraic tensor thermal diffusivity models, and later in §2.3 the hierarchical relationships between these models will be addressed in greater detail.

In order to obtain deeper insights for constructing an improved SGS HF model for LES, previous experience garnered from various developments in the Reynolds-averaged Navier–Stokes (RANS) method and in the area of continuum physics have proven to be very useful. Daly & Harlow (1970) proposed a so-called generalized gradient diffusion hypothesis (GGDH) for building turbulent heat flux models for the RANS approach. In comparison with the conventional eddy diffusivity approach,

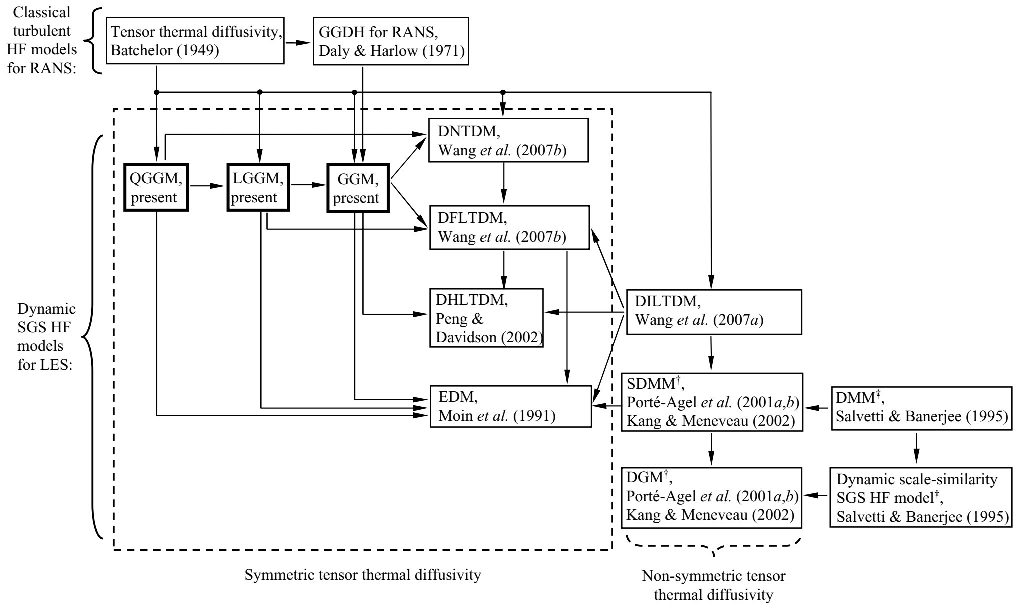

FIGURE 1. Relationships between the classical turbulent HF models for RANS and dynamic SGS HF models for LES within the framework of the explicit algebraic modelling approach. The relationships between the existing models and proposed models addressed in §2.3 are highlighted using the large dashed-line box, all of which involve real symmetrical tensor thermal diffusivities. †The concept for the DGM, namely

$$h_j^{DG} = -D_{jk}^{DG}\frac{\partial\bar{\theta}}{\partial x_k} = -C_\theta\bar{\Delta}^2\bar{A}_{jk}\frac{\partial\bar{\theta}}{\partial x_k} = -C_\theta\bar{\Delta}^2\frac{\partial\bar{u}_j}{\partial x_k}\frac{\partial\bar{\theta}}{\partial x_k},$$

originates from the dynamic gradient SGS stress model of Clark *et al.* (1979). The SDMM is built by mixing h_j^{DG} with an eddy thermal diffusivity model. Here, C_θ is a dynamic model coefficient. ‡The concept for a dynamic scale-similarity SGS HF model, namely,

$$h_j^S = C_\theta(\overline{\bar{u}_j\bar{\theta}} - \bar{\bar{u}}_j\bar{\bar{\theta}}),$$

originates from the dynamic scale-similarity SGS stress model of Bardina *et al.* (1980). The DMM is built by mixing h_j^S with an eddy thermal diffusivity model.

the proposed GGDH approach relates the tensor diffusivity linearly to the Reynolds stress tensor, which in turn offers more degrees of freedom for modelling the turbulent heat flux. Furthermore, the design of a turbulent HF model in the GGDH approach is versatile owing to the availability of increasingly sophisticated Reynolds stress models contributed by several generations of researchers. In continuum physics, the theory of tensor invariants and functions is essential for modelling the nonlinear constitutive relations required for describing crystal classes, viscoelastic phenomena and non-Newtonian fluids. Modern development of rigorous formulations for nonlinear constitutive laws using tensor functions derives largely from the pioneering efforts of Reiner (1945) and Rivlin (1948). Since this seminal work, the mathematical theory of tensor invariants and functions and its application to the formulation of nonlinear constitutive relations have been extensively developed (see Spencer 1971; Zheng 1994). The application of tensor invariants and functions for the construction of algebraic turbulent stress models within the RANS approach was systematically investigated by Lumley (1970), and further advanced by Pope (1975) and Rodi (1976). Since then, tensor invariants and functions have been applied to the construction of RANS algebraic turbulent HF models for studying thermal convection. Recent advancements in this area of RANS modelling have been the subject of a number of comprehensive reviews (So & Speziale 1999; Hanjalić 2002; Younis, Speziale & Clark 2005).

Previous approaches for dynamic SGS HF modelling, as represented by the EDM (Moin *et al.* 1991), DGM and DMM (Salvetti & Banerjee 1995; Porté-Agel *et al.* 2001*a*,*b*), DHLTDM (Peng & Davidson 2002), DILTDM (Wang *et al.* 2007*a*), and DFLTDM and DNTDM (Wang *et al.* 2007*b*) are based on the resolved velocity gradient tensor $\bar{A}_{ij}$ (or its symmetrical and asymmetrical components, i.e. the resolved strain rate tensor $\bar{S}_{ij}$ and the rotation rate tensor $\bar{\Omega}_{ij}$, respectively) for the construction of the constitutive relations. In contrast to these previous investigations, the objective of the current research is to use the theory of tensor functions (Spencer 1971; Zheng 1994) to extend the concept of GGDH from the context of RANS to that of LES to develop three new dynamic tensor diffusivity SGS HF models based on the SGS stress tensor τ_{ij}. One of the most attractive features of the present new modelling approach is that because the tensor diffusivity for the three proposed models is a tensor function (linear or nonlinear) of τ_{ij}, a number of explicit algebraic SGS stress models proposed previously by various researchers can be utilized for constructing the SGS HF models. As such, the model for the SGS HF vector has more degrees of freedom (dependent on the choice of the SGS stress model) with the result that the concomitant constitutive relationship achieves greater generality in comparison with the conventional approaches.

This paper is organized as follows: in §2, formulations for the SGS stress and HF models are introduced; in §3, the test cases and numerical algorithm are described; in §4, the results for LES of neutrally and unstably stratified flows are analysed; and finally in §5, the major conclusions of this research are summarized.

2. SGS stress and heat flux models

In LES of thermal convection, the filtered continuity, momentum and scalar transport equations together form the system of governing equations for determining the filtered velocity and scalar (temperature) fields, which take the following form for an incompressible flow:

$$\frac{\partial \bar{u}_i}{\partial x_i} = 0, \tag{2.1}$$

$$\frac{\partial \bar{u}_i}{\partial t} + \frac{\partial}{\partial x_j}(\bar{u}_i \bar{u}_j) = -\frac{1}{\rho}\frac{\partial \bar{p}}{\partial x_i} + \nu \frac{\partial^2 \bar{u}_i}{\partial x_j \partial x_j} - \frac{\partial \tau_{ij}}{\partial x_j} - \beta g_i(\bar{\theta} - \Theta_r), \tag{2.2}$$

$$\frac{\partial \bar{\theta}}{\partial t} + \frac{\partial}{\partial x_j}(\bar{u}_j \bar{\theta}) = \alpha \frac{\partial^2 \bar{\theta}}{\partial x_j \partial x_j} - \frac{\partial h_j}{\partial x_j}, \tag{2.3}$$

where $\bar{\theta}$ represents the filtered temperature, $[g_i] = [0, -g, 0]^T$ is the gravitational acceleration vector, ρ is the density of the fluid (air), ν is the kinematic viscosity, β is the thermal expansion coefficient, α is the molecular thermal diffusivity, and Θ_r is a reference temperature, which for our test case of an unstably stratified channel flow, is taken as the bulk temperature, i.e.

$$\Theta_r = \theta_B = \int_0^{2\delta} \langle \bar{\theta} \rangle \mathrm{d}x_2 / 2\delta.$$

Here, δ is the half-channel width, and $\langle \cdot \rangle$ corresponds to a quantity averaged both in time and over the homogeneous (x_1, x_3)-plane. The streamwise, wall-normal and

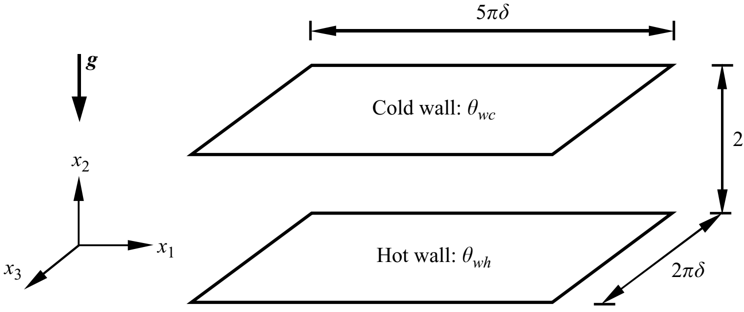

FIGURE 2. Physical domain for an unstably stratified flow in a horizontal channel.

spanwise coordinates for the Cartesian frame are denoted using x_1, x_2 and x_3, respectively (see figure 2). As a consequence of the filtering process, the so-called SGS stress tensor and SGS HF vector appear in the above system of governing equations, and are defined as

$$\tau_{ij} \stackrel{\mathrm{def}}{=} \overline{u_i u_j} - \bar{u}_i \bar{u}_j$$

and

$$h_j \stackrel{\mathrm{def}}{=} \overline{u_j \theta} - \bar{u}_j \bar{\theta},$$

respectively. In the following two Subsections, the conventional and proposed modelling formulations for τ_{ij} and h_j, required for closing the above system of governing equations, are described.

2.1. *SGS stress models*

Two dynamic SGS stress models are used: namely, the conventional dynamic Smagorinsky model (DM) of Lilly (1992) and dynamic nonlinear SGS stress model (DNM) of Wang & Bergstrom (2005). The following text briefly describes these two dynamic SGS stress models.

SGS stress model 1 (DM)

The constitutive relation for the DM is based on a tensor function of the resolved strain rate tensor $\bar{S}_{ij}$,

$$\tau_{ij}^* = \tau_{ij} - \frac{\tau_{kk}}{3}\delta_{ij} = -2C_S\bar{\Delta}^2|\bar{\boldsymbol{S}}|\bar{S}_{ij}, \tag{2.4}$$

where $|\bar{\boldsymbol{S}}| = (2\bar{S}_{ij}\bar{S}_{ji})^{1/2}$ is the norm of the resolved strain rate tensor, $\bar{\Delta}$ is the grid-level filter width, δ_{ij} is the Kronecker delta, and an asterisk represents a trace-free tensor, i.e. $(\cdot)_{ij}^* \stackrel{\mathrm{def}}{=} (\cdot)_{ij} - (\cdot)_{kk}\delta_{ij}/3$. The SGS eddy viscosity implied in (2.4) is $\nu_{sgs} = C_S\bar{\Delta}^2|\bar{\boldsymbol{S}}|$, and therefore, this model can be further simplified as $\tau_{ij}^* = -2\nu_{sgs}\bar{S}_{ij}$. By minimizing the residual of the Germano identity following the dynamic procedure of Lilly (1992), the model coefficient C_S can be obtained as

$$C_S = -\frac{M_{ij}\mathscr{L}_{ij}}{M_{mn}M_{mn}}, \tag{2.5}$$

where $\mathscr{L}_{ij} \stackrel{\mathrm{def}}{=} \widetilde{\bar{u}_i\bar{u}_j} - \tilde{\bar{u}}_i\tilde{\bar{u}}_j$ is the resolved Leonard-type stress; and $M_{ij} \stackrel{\mathrm{def}}{=} \alpha_{ij} - \tilde{\beta}_{ij}$ is a differential tensor with $\alpha_{ij} \stackrel{\mathrm{def}}{=} 2\tilde{\bar{\Delta}}^2|\tilde{\bar{\boldsymbol{S}}}|\tilde{\bar{S}}_{ij}$ and $\beta_{ij} \stackrel{\mathrm{def}}{=} 2\bar{\Delta}^2|\bar{\boldsymbol{S}}|\bar{S}_{ij}$. In these equations, the filtered quantities at the grid level are denoted using an overbar, while the filtered quantities at the test-grid level for the dynamic procedure are denoted using a tilde. Following the usual convention, the grid-level filter width is considered as the grid size itself, whereas the test-grid-level filter width for the dynamic procedure is set to twice the grid size.

SGS stress model 2 (DNM)

The constitutive relation for the DNM is based on an explicit nonlinear quadratic tensorial polynomial constitutive relation originally proposed by Speziale (1987) (see also Gatski & Speziale 1993) for modelling of the Reynolds stress tensor in a RANS approach. By analogy, the SGS stress tensor can be modelled using the following functional form within the context of an LES approach:

$$\tau^*_{ij} = -C_S\beta_{ij} - C_W\gamma_{ij} - C_N\eta_{ij}. \tag{2.6}$$

The definition of β_{ij} remains unchanged and the other two base tensor functions are defined as $\gamma_{ij} \overset{\text{def}}{=} 4\bar{\Delta}^2(\bar{S}_{ik}\bar{\Omega}_{kj} + \bar{S}_{jk}\bar{\Omega}_{ki})$ and $\eta_{ij} \overset{\text{def}}{=} 4\bar{\Delta}^2(\bar{S}_{ik}\bar{S}_{kj} - \bar{S}_{mn}\bar{S}_{nm}\delta_{ij}/3)$, respectively. It can be shown (Wang & Bergstrom 2005) that the values of the three model coefficients C_S, C_W and C_N can be obtained by minimizing the residual of the Germano identity following the dynamic procedure of Lilly (1992) as

$$\begin{bmatrix} M_{ij}M_{ij} & M_{ij}W_{ij} & M_{ij}N_{ij} \\ W_{ij}M_{ij} & W_{ij}W_{ij} & W_{ij}N_{ij} \\ N_{ij}M_{ij} & N_{ij}W_{ij} & N_{ij}N_{ij} \end{bmatrix} \cdot \begin{bmatrix} C_S \\ C_W \\ C_N \end{bmatrix} = - \begin{bmatrix} \mathscr{L}^*_{ij}M_{ij} \\ \mathscr{L}^*_{ij}W_{ij} \\ \mathscr{L}^*_{ij}N_{ij} \end{bmatrix}. \tag{2.7}$$

Here, the definition of M_{ij} remains unchanged and the other two differential tensors are defined as $W_{ij} \overset{\text{def}}{=} \lambda_{ij} - \tilde{\gamma}_{ij}$ and $N_{ij} \overset{\text{def}}{=} \zeta_{ij} - \tilde{\eta}_{ij}$, respectively, with $\lambda_{ij} \overset{\text{def}}{=} 4\tilde{\bar{\Delta}}^2(\tilde{\bar{S}}_{ik}\tilde{\bar{\Omega}}_{kj} + \tilde{\bar{S}}_{jk}\tilde{\bar{\Omega}}_{ki})$ and $\zeta_{ij} \overset{\text{def}}{=} 4\tilde{\bar{\Delta}}^2(\tilde{\bar{S}}_{ik}\tilde{\bar{S}}_{kj} - \tilde{\bar{S}}_{mn}\tilde{\bar{S}}_{nm}\delta_{ij}/3)$.

The design of the constitutive relation (2.6), in terms of the choice of the three constituent tensorial base components (i.e. β_{ij}, γ_{ij} and η_{ij}) is not arbitrary: (i) the first term β_{ij} is the well-known Smagorinsky component which primarily relates to the SGS dissipation and forwardscatter of turbulent kinetic energy (TKE) from the resolved to subgrid-scale motions; (ii) the second term γ_{ij} does not make any contribution to the TKE transfer between the resolved and subgrid scales, but according to a recent systematic *a priori* LES study of Horiuti (2003), it significantly improves the correlation between the exact τ_{ij} extracted from a direct numerical simulation (DNS) database and that predicted by the nonlinear model; and, (iii) as demonstrated previously (Wang & Bergstrom 2005; Wang *et al.* 2006*a*), the third term η_{ij} contributes significantly to the backscatter of TKE from the subgrid to the resolved scales. The three features mentioned here are among the most important criteria for evaluation of a successful SGS stress model. Speziale's constitutive relation, on which the DNM is based, offers an effective representation to model individually these three important physical features using three independent terms. Further applications of the DNM can be found in Wang *et al.* (2006*a*) on the study of the topological features of wall-bounded turbulent flows and in Wang, Yee & Bergstrom (2006*b*, 2008) on the study the geometrical properties of the SGS stress tensor and resolved vorticity vector.

2.2. *SGS heat flux models*

The focus of this research is on modelling the SGS HF, rather than the SGS stress. For this purpose, we propose three new dynamic models and relate them to existing SGS HF models. In order to perform a comparative study, the three proposed SGS HF models are tested against the conventional EDM. All the SGS HF models investigated in this study can be categorized under the general framework of tensor thermal diffusivity HF modelling originally introduced by Batchelor (1949), who suggested the following model for representing the turbulent HF vector $\langle u'_j\theta'\rangle_e$ in a RANS approach:

$$\langle u'_j\theta'\rangle_e = -D_{jk}\frac{\partial\langle\theta\rangle_e}{\partial x_k}, \tag{2.8}$$

where D_{jk} is the so-called turbulent tensor thermal diffusivity, and $\langle\cdot\rangle_e$ represents an ensemble-averaged quantity in a RANS approach. An important application of Batchelor's suggestion is the GGDH model proposed by Daly & Harlow (1970), which models the turbulent tensor thermal diffusivity linearly in terms of the Reynolds stresses and expresses the turbulent HF vector as

$$\langle u'_j\theta'\rangle_e = -C_\theta\mathscr{T}_e\langle u'_ju'_k\rangle_e\frac{\partial\langle\theta\rangle_e}{\partial x_k}, \tag{2.9}$$

where C_θ is a model coefficient, $\mathscr{T}_e$ is an appropriate turbulent time scale, $\langle u'_ju'_k\rangle_e$ is the Reynolds stress tensor, and the turbulent tensor thermal diffusivity is defined as $D_{jk} = C_\theta\mathscr{T}_e\langle u'_ju'_k\rangle_e$. The idea of using the GGDH approach of Daly & Harlow (1970) to formulate a constitutive relation for modelling the SGS HF vector in the context of LES has been briefly mentioned in Peng & Davidson (2002). In the remainder of this Subsection, we summarize the formulation of four SGS HF models, which include the conventional EDM and our three proposed SGS HF models. We will also demonstrate that our three proposed models correspond to generalized formulations for the SGS HF vector in the sense that they include a number of conventional dynamic SGS HF models as special cases, such as the EDM, DHLTDM, DFLTDM and DNTDM.

SGS heat flux model 1 (EDM)

The EDM model proposed by Moin *et al.* (1991) expresses the SGS heat flux as

$$h_j = -C_\theta\bar{\Delta}^2|\bar{\boldsymbol{S}}|\frac{\partial\bar{\theta}}{\partial x_j}, \tag{2.10}$$

where the scalar eddy diffusivity implied by (2.10) is $\alpha_{sgs} = C_\theta\bar{\Delta}^2|\bar{\boldsymbol{S}}|$, which can be further written in a general tensor diffusivity form using the Kronecker delta as follows:

$$D^E_{jk} = \alpha_{sgs}\delta_{jk} = C_\theta\bar{\Delta}^2|\bar{\boldsymbol{S}}|\delta_{jk}. \tag{2.11}$$

In view of this, (2.10) can be re-cast as $h_j = -D^E_{jk}\partial\bar{\theta}/\partial x_k$. Introducing the grid-level and test-grid-level base vector functions as $b_j \overset{\text{def}}{=} \bar{\Delta}^2|\bar{\boldsymbol{S}}|\partial\bar{\theta}/\partial x_j$ and $a_j \overset{\text{def}}{=} \tilde{\bar{\Delta}}^2|\tilde{\bar{\boldsymbol{S}}}|\partial\tilde{\bar{\theta}}/\partial x_j$, the SGS HF vector at the grid level as represented by (2.10) can then be expressed as $h_j = -C_\theta b_j$. Similarly, the SGS HF vector at the test-grid level ($H_j \overset{\text{def}}{=} \widetilde{\overline{u_j\theta}} - \tilde{\bar{u}}_j\tilde{\bar{\theta}}$) can be expressed as $H_j = -C_\theta a_j$. The grid- and test-grid-level SGS HF vectors satisfy the vector identity:

$$\mathscr{L}_j = H_j - \tilde{h}_j, \tag{2.12}$$

where $\mathscr{L}_j \overset{\text{def}}{=} \widetilde{\bar{u}_j\bar{\theta}} - \tilde{\bar{u}}_j\tilde{\bar{\theta}}$ is a resolved heat flux vector directly computable in the simulation. By substituting the grid- and test-grid-level SGS HF models into the vector identity and assuming that $\tilde{h}_j = -\widetilde{C_\theta b_j} \approx -C_\theta\tilde{b}_j$, a residual vector that expresses the difference between the left-hand side and right-hand side of the vector identity emerges:

$$\mathscr{E}_j = \mathscr{L}_j + C_\theta(a_j - \tilde{b}_j) = \mathscr{L}_j + C_\theta M_j, \tag{2.13}$$

where $M_j \overset{\text{def}}{=} a_j - \tilde{b}_j$ is a differential vector. By minimizing the norm of the residual of the vector identity (i.e. $\mathscr{E} \overset{\text{def}}{=} \mathscr{E}_j\mathscr{E}_j$) using the least-squares method, the model coefficient C_θ can be obtained,

$$C_\theta = -\frac{\mathscr{L}_j M_j}{M_i M_i}. \tag{2.14}$$

SGS heat flux model 2 (GGM)

The original constitutive relation of Daly & Harlow (1970) is based on the Reynolds stress tensor for modelling the turbulent heat flux within the RANS approach. In the context of LES, this constitutive relation results in

$$h_j = -C_{\theta G}\mathscr{T}\tau_{jk}\frac{\partial\bar{\theta}}{\partial x_k}. \tag{2.15}$$

In an LES approach, it is conventional for the isotropic part of τ_{ij} (i.e. $\tau_{kk}\delta_{ij}/3$) to be incorporated with the filtered pressure term $\bar{p}$, with the result that only the trace-free SGS stress tensor τ^*_{ij} is modelled. Therefore, in a conventional LES approach, (2.15) is simplified to

$$h_j = -C_{\theta G}\mathscr{T}\tau^*_{jk}\frac{\partial\bar{\theta}}{\partial x_k}, \tag{2.16}$$

where $\mathscr{T}$ is a characteristic subgrid time scale which is evaluated using the norm of the resolved velocity gradient tensor $\bar{A}_{ij}$, i.e. $\mathscr{T} = 1/|\bar{\boldsymbol{A}}|$ (or optionally using the norm of the resolved strain rate tensor as $\mathscr{T} = 1/|\bar{\boldsymbol{S}}|$). The norm of the resolved velocity gradient tensor is defined as $|\bar{\boldsymbol{A}}| \overset{\text{def}}{=} (2\bar{A}_{ij}\bar{A}_{ij})^{1/2} = (2\bar{S}_{ij}\bar{S}_{ij} + 2\bar{\Omega}_{ij}\bar{\Omega}_{ij})^{1/2} = (|\bar{\boldsymbol{S}}|^2 + |\bar{\boldsymbol{\Omega}}|^2)^{1/2}$. Equations (2.15) and (2.16) form the constitutive relations for our proposed dynamic GGDH model for representing the SGS heat flux (GGM). From (2.16), the tensor diffusivity for the GGM can be inferred as

$$D^G_{jk} = f(\tau^*_{jk}) = C_{\theta G}\mathscr{T}\tau^*_{jk}, \tag{2.17}$$

which is a homogenous linear tensor function of τ^*_{jk}. Here, homogeneity derives from a terminology used in linear algebra, in which a linear transformation that satisfies the condition $D^G_{jk} = f(\tau^*_{jk}) = 0$ if $\tau^*_{jk} = 0$ is referred to as being homogeneous.

By using the norm of the resolved velocity gradient tensor for evaluating the SGS time scale at both the grid and test-grid levels, and defining the base vector functions as

$$b^G_j \overset{\text{def}}{=} \frac{\tau^*_{jk}}{|\bar{\boldsymbol{A}}|}\frac{\partial\bar{\theta}}{\partial x_k} \quad \text{and} \quad a^G_j \overset{\text{def}}{=} \frac{T^*_{jk}}{|\tilde{\bar{\boldsymbol{A}}}|}\frac{\partial\tilde{\bar{\theta}}}{\partial x_k}, \tag{2.18}$$

the grid and test-grid level SGS HF vectors can then be expressed succinctly as $h_j = -C_{\theta G}\, b^G_j$ and $H_j = -C_{\theta G}\, a^G_j$, respectively. Here $T^*_{jk} \overset{\text{def}}{=} (\widetilde{\bar{u}_j\bar{u}_k} - \tilde{\bar{u}}_j\tilde{\bar{u}}_k)^*$ represents the trace-free SGS stress tensor at the test-grid level. Similarly, the optimal model coefficient $C_{\theta G}$ can be obtained by minimizing the residual of the vector identity using the least squares method,

$$C_{\theta G} = -\frac{\mathscr{L}_j G_j}{G_i G_i}, \tag{2.19}$$

where $G_j \overset{\text{def}}{=} a^G_j - \tilde{b}^G_j$ is a differential vector.

It should be noted that the two modelling approaches represented by (2.15) and (2.16) are slightly different, in that the tensor diffusivity for the latter is trace-free (i.e. $\text{tr}(D^G_{jk}) = \text{tr}(C_{\theta G}\mathscr{T}\tau^*_{jk}) = 0$). In consequence, the local instantaneous value of D^G_{jk}

is not guaranteed to be positive definite. This can result in a backscatter of scalar energy from the subgrid to resolved scales. Later in §4.3, we will explore this subject in greater detail.

SGS heat flux model 3 (LGGM)

As demonstrated earlier, the tensor diffusivity for the EDM is a function of $\bar{S}_{ij}$ of the zeroth order (i.e. $D^E_{jk} = C_\theta \bar{\Delta}^2 |\bar{\boldsymbol{S}}| \delta_{jk}$). Within the framework of constitutive relations of the form $h_j = f(\tau^*_{ij}, \partial\bar{\theta}/\partial x_j)$, a tensor diffusivity of the zeroth order can be analogously constructed as $D^P_{jk} = C_{\theta P} \mathscr{T} |\boldsymbol{\tau}| \delta_{jk}$. The tensor diffusivity for the GGM based on the original GGDH approach of Daly & Harlow (1970) is a homogeneous linear function of τ^*_{ij} of the first order (i.e. $D^G_{jk} = C_{\theta G} \mathscr{T} \tau^*_{jk}$). According to the theory of tensor polynomial functions, a full linear tensor diffusivity function of τ^*_{jk} consists of both zeroth- and first-order parts. Therefore, we can extend the GGDH constitutive relation of Daly & Harlow (1970) from a homogeneous linear tensor function to an inhomogeneous full linear tensor function as follows:

$$\begin{aligned} D^L_{jk} &= D^P_{jk} + D^G_{jk} \\ &= C_{\theta P} \mathscr{T} |\boldsymbol{\tau}| \delta_{jk} + C_{\theta G} \mathscr{T} \tau^*_{jk}. \end{aligned} \tag{2.20}$$

This corresponds to the following constitutive relation for our proposed full linear dynamic GGDH model (LGGM) for representing the SGS heat flux:

$$\begin{aligned} h_j &= -D^L_{jk} \frac{\partial \bar{\theta}}{\partial x_k} \\ &= -C_{\theta P} \mathscr{T} |\boldsymbol{\tau}| \frac{\partial \bar{\theta}}{\partial x_j} - C_{\theta G} \mathscr{T} \tau^*_{jk} \frac{\partial \bar{\theta}}{\partial x_k}. \end{aligned} \tag{2.21}$$

Introduce the base vector functions

$$b^P_j \overset{\text{def}}{=} \frac{|\boldsymbol{\tau}|}{|\bar{\boldsymbol{A}}|} \frac{\partial \bar{\theta}}{\partial x_j} \quad \text{and} \quad a^P_j \overset{\text{def}}{=} \frac{|\boldsymbol{T}|}{|\tilde{\bar{\boldsymbol{A}}}|} \frac{\partial \tilde{\bar{\theta}}}{\partial x_j}, \tag{2.22}$$

where $|\boldsymbol{\tau}| \overset{\text{def}}{=} (2\tau^*_{ij}\tau^*_{ij})^{1/2}$ and $|\boldsymbol{T}| = (2T^*_{ij}T^*_{ij})^{1/2}$ are the norms of the SGS stress tensor at the grid and test-grid levels, respectively. With these definitions, the grid- and test-grid-level SGS HF vectors can be simplified to $h_j = -C_{\theta P} b^P_j - C_{\theta G} b^G_j$ and $H_j = -C_{\theta P} a^P_j - C_{\theta G} a^G_j$, respectively. The dynamic model coefficients $C_{\theta P}$ and $C_{\theta G}$ can be obtained by minimizing the residual ($\mathscr{E}$) of the vector identity using the least-squares method. It can be shown by setting $\partial\mathscr{E}/\partial C_{\theta P} = 0$ and $\partial\mathscr{E}/\partial C_{\theta G} = 0$ that the following system of equations for computing the model coefficients is obtained:

$$\begin{bmatrix} P_j P_j & P_j G_j \\ G_j P_j & G_j G_j \end{bmatrix} \cdot \begin{bmatrix} C_{\theta P} \\ C_{\theta G} \end{bmatrix} = - \begin{bmatrix} \mathscr{L}_j P_j \\ \mathscr{L}_j G_j \end{bmatrix}, \tag{2.23}$$

where $P_j \overset{\text{def}}{=} a^P_j - \tilde{b}^P_j$ is a differential vector.

SGS heat flux model 4 (QGGM)

According to the theory of tensor invariants and functions, a vector-valued function of a second-order symmetric tensor $\boldsymbol{M}$ and a vector $\boldsymbol{v}$ can be represented by Noll's formula (Zheng 1994) as follows:

$$\boldsymbol{h} = \varphi_0 \boldsymbol{v} + \varphi_1 \boldsymbol{M} \boldsymbol{v} + \varphi_2 \boldsymbol{M}^2 \boldsymbol{v}, \tag{2.24}$$

where φ_i $(i = 0, 1, 2)$ are coefficients of the form $\varphi_i = \varphi_i(I_M, II_M, III_M, I_v, I_{Mv}, II_{Mv})$. Here, $I_M = \mathrm{tr}(\boldsymbol{M})$, $II_M = \mathrm{tr}(\boldsymbol{M}^2)$ and $III_M = \mathrm{tr}(\boldsymbol{M}^3)$ are the three independent invariants of $\boldsymbol{M}$; $I_v = \boldsymbol{v} \cdot \boldsymbol{v}$ is the invariant of $\boldsymbol{v}$; and $I_{Mv} = \boldsymbol{v} \cdot \boldsymbol{M}\boldsymbol{v}$ and $II_{Mv} = \boldsymbol{v} \cdot \boldsymbol{M}^2\boldsymbol{v}$ are the two independent invariants for $\boldsymbol{M}$ and $\boldsymbol{v}$. Noll's formula provides an explicit, inhomogeneous, complete and irreducible tensor function of $\boldsymbol{M}$ and $\boldsymbol{v}$, forming the basis for our proposed quadratic dynamic GGDH model (QGGM) for representing the SGS heat flux:

$$\begin{aligned} h_j &= -D^Q_{jk}\frac{\partial\bar{\theta}}{\partial x_k} \\ &= -C_{\theta P}\mathscr{T}|\boldsymbol{\tau}|\frac{\partial\bar{\theta}}{\partial x_j} - C_{\theta G}\mathscr{T}\tau^*_{jk}\frac{\partial\bar{\theta}}{\partial x_k} - C_{\theta Q}\mathscr{T}\frac{\tau^*_{ji}\tau^*_{ik}}{|\boldsymbol{\tau}|}\frac{\partial\bar{\theta}}{\partial x_k}, \end{aligned} \tag{2.25}$$

where the tensor diffusivity is a quadratic nonlinear tensor function of τ^*_{ij},

$$D^Q_{jk} = C_{\theta P}\mathscr{T}|\boldsymbol{\tau}|\delta_{jk} + C_{\theta G}\mathscr{T}\tau^*_{jk} + C_{\theta Q}\mathscr{T}\frac{\tau^*_{ji}\tau^*_{ik}}{|\boldsymbol{\tau}|}. \tag{2.26}$$

The three terms on the right-hand side of (2.25) are identified as: the zeroth-order tensor diffusivity (or eddy diffusivity) component (similar to the conventional EDM, or Model 1); the first-order homogeneous tensor diffusivity component (corresponding to the GGM, or Model 2); and the quadratic nonlinear tensor diffusivity component. Equations (2.24) and (2.25) are inhomogeneous owing to the presence of the SGS eddy diffusivity term (the term related to δ_{jk}), irreducible because none of $\boldsymbol{v}$, $\boldsymbol{M}\boldsymbol{v}$ and $\boldsymbol{M}^2\boldsymbol{v}$ can be expressed as a single-valued function of the remaining terms, and complete because any vector function of the form $\boldsymbol{h} = f(\boldsymbol{M}, \boldsymbol{v})$ can be expressed by (2.24). As such, no higher-order terms (e.g. terms related to $\tau^*_{ji}\tau^*_{il}\tau^*_{lk}\partial\bar{\theta}/\partial x_k$) should appear in (2.25), since these are not independent of the existing terms.

Introduce the base vector functions

$$b^Q_j \overset{\text{def}}{=} \frac{\tau^*_{ji}\tau^*_{ik}}{|\boldsymbol{\tau}||\bar{\boldsymbol{A}}|}\frac{\partial\bar{\theta}}{\partial x_k} \quad \text{and} \quad a^Q_j \overset{\text{def}}{=} \frac{T^*_{ji}T^*_{ik}}{|\boldsymbol{T}||\tilde{\bar{\boldsymbol{A}}}|}\frac{\partial\tilde{\bar{\theta}}}{\partial x_k}. \tag{2.27}$$

The grid-level SGS HF can be simplified as

$$h_j = -C_{\theta P}b^P_j - C_{\theta G}b^G_j - C_{\theta Q}b^Q_j. \tag{2.28}$$

Similarly, the constitutive relation for the SGS HF at the test-grid level can be expressed as

$$H_j = -C_{\theta P}a^P_j - C_{\theta G}a^G_j - C_{\theta Q}a^Q_j. \tag{2.29}$$

By substituting (2.28) and (2.29) into the vector identity (i.e. (2.12)), a 3 × 3 matrix system for computing the model coefficients can be directly obtained as

$$[P_j, G_j, Q_j] \cdot [C_{\theta P}, C_{\theta G}, C_{\theta Q}]^T = -\mathscr{L}_j, \tag{2.30a}$$

for $j = 1$, 2 and 3; or equivalently,

$$\begin{bmatrix} P_1 & G_1 & Q_1 \\ P_2 & G_2 & Q_2 \\ P_3 & G_3 & Q_3 \end{bmatrix} \cdot \begin{bmatrix} C_{\theta P} \\ C_{\theta G} \\ C_{\theta Q} \end{bmatrix} = -\begin{bmatrix} \mathscr{L}_1 \\ \mathscr{L}_2 \\ \mathscr{L}_3 \end{bmatrix}. \tag{2.30b}$$

For brevity, we use $\boldsymbol{K} \cdot \boldsymbol{c} = -\boldsymbol{l}$ to denote this linear system of equations. Here, $Q_j \overset{\text{def}}{=} a^Q_j - \tilde{b}^Q_j$ is a differential vector, and the definitions of P_j and G_j remain unchanged.

In the derivation of (2.30*a*), we made use of an assumption analogous to that adopted in the dynamic procedure of Lilly (1992): $C_{\theta P} b_j^P \approx C_{\theta P} \tilde{b}_j^P$, $C_{\theta G} b_j^G \approx C_{\theta G} \tilde{b}_j^G$ and $C_{\theta Q} b_j^Q \approx C_{\theta Q} \tilde{b}_j^Q$.

It should be noted that (2.30*a*) (or (2.30*b*)) derives directly from the vector identity (i.e. (2.12)), without having to apply the least-squares approach, which is a unique feature for a dynamic SGS HF model with three coefficients. Left-multiplying both sides of (2.30*a*) by $\boldsymbol{K}^T$, we obtain the following matrix system:

$$(\boldsymbol{K}^T \boldsymbol{K}) \cdot \boldsymbol{c} = -\boldsymbol{K}^T \cdot \boldsymbol{l}. \tag{2.31}$$

Equation (2.31) can be used as an alternative to (2.30*a*) for computing the model coefficients. Equation (2.31) can also be obtained using the least-squares approach by setting $\partial \mathscr{E} / \partial C_{\theta P} = \partial \mathscr{E} / \partial C_{\theta G} = \partial \mathscr{E} / \partial C_{\theta Q} = 0$, where $\mathscr{E} = \mathscr{E}_j \mathscr{E}_j$ and $\mathscr{E}_j$ is the residual vector which in this case takes the following form:

$$\begin{aligned} \mathscr{E}_j &= \mathscr{L}_j + C_{\theta P}\left(a_j^P - \tilde{b}_j^P\right) + C_{\theta G}\left(a_j^G - \tilde{b}_j^G\right) + C_{\theta Q}\left(a_j^Q - \tilde{b}_j^Q\right) \\ &= \mathscr{L}_j + C_{\theta P} P_j + C_{\theta G} G_j + C_{\theta Q} Q_j. \end{aligned} \tag{2.32}$$

The differential vectors P_j, G_j and Q_j are linearly independent tensor functions. This is because b_j^P, b_j^G and b_j^Q are linearly independent functions of τ_{ij}^* and $\partial \bar{\theta} / \partial x_j$; a_j^P, a_j^G and a_j^Q are linearly independent functions of T_{ij}^* and $\partial \tilde{\bar{\theta}} / \partial x_j$; and τ_{ij}^* and T_{ij}^* are two independent tensor variables related by the Germano identity. This is a desirable mathematical property for both (2.30*a*) and (2.31) in terms of the numerical stability. However, owing to the complexity of the problem and physics of the turbulent flow, the numerical stability of a modelling approach cannot be entirely diagnosed using an *a priori* mathematical analysis, and indeed, needs to be confirmed by conducting numerical simulations. From the numerical tests performed in this study, it is observed that both (2.30*a*) and (2.31) can be applied to compute the model coefficients without encountering any numerical instability. The numerical results presented in this paper were obtained using (2.30*a*), rather than (2.31).

From the numerical simulations conducted here, we observed that the DNM is numerically more robust than the DM. The DNM can be applied locally at each time step of the flow simulation without resorting to any form of plane-averaging for a stable computation of the model coefficients. In contrast, when the DM was applied to modelling the SGS stress, it was always necessary to use plane-averaging to achieve numerical stability. This observation is consistent with our previous experience (Wang & Bergstrom 2005), which thoroughly investigated the numerical stability of the DNM and DM based on a turbulent Couette flow. Since the focus of the current research is on the SGS HF models, we now discuss the numerical stability of the proposed SGS HF models. For the proposed GGM (cf. (2.19)), LGGM (cf. (2.23)) and QGGM (cf. (2.30*a*)), we observed that these formulations can also be applied locally at each time step without using plane-averaging for a stable computation of the model coefficients, if the DNM is used for constructing their constitutive relations. This desirable feature of the models is related to the utilization of a tensor diffusivity in the construction of their constitutive relations. When the DNM (which is a quadratic tensor function of $\bar{S}_{ij}$ and $\bar{\Omega}_{ij}$) is used, the constitutive relations of our three proposed SGS HF models (GGM, LGGM and QGGM) become higher-order (second-order and above) complex tensor functions of $\bar{S}_{ij}$, $\bar{\Omega}_{ij}$ and $\partial \bar{\theta} / \partial x_j$. The greater complexity (and concomitant flexibility) of these proposed SGS HF models leads generally to a smaller probability for the determinant of the coefficient matrix of (2.19) for the GGM, (2.23) for the LGGM, and (2.30*a*) for the QGGM to vanish identically in comparison to that for the

Acronym	Description	References
EDM	linear eddy thermal diffusivity model	Moin *et al.* (1991)
DSSM	scale-similarity SGS HF model	Salvetti & Banerjee (1995)
DMM	two-parameter mixed SGS HF model	Salvetti & Banerjee (1995)
SDMM	simplified DMM	Porté-Agel *et al.* (2001*a*,*b*) Kang & Meneveau (2002)
DGM	gradient SGS HF model	Porté-Agel *et al.* (2001*a*,*b*) Kang & Meneveau (2002)
DHLTDM	homogeneous linear tensor diffusivity model	Peng & Davidson (2002)
DILTDM	inhomogeneous linear tensor diffusivity model	Wang *et al.* (2007*a*)
DFLTDM	full linear tensor diffusivity model	Wang *et al.* (2007*b*)
DNTDM	nonlinear tensor diffusivity model	Wang *et al.* (2007*b*)
GGM	GGDH SGS HF model	present
LGGM	full linear GGDH SGS HF model	present
QGGM	quadratic GGDH SGS HF model	present

TABLE 1. Summary of the relevant dynamic SGS HF models. See figure 1 for the relationships between the above SGS HF models and annotations on the references relevant to the dynamic scale-similarity, gradient and mixed SGS HF models.

determinant of the coefficient matrix of (2.14) for the EDM. This is expected to lead to a greater stability in the application of the GGM, LGGM and QGGM relative to that of the EDM, which is consistent with our current experience in the application of these models to the two test flow problems studied in this paper. Nevertheless, it remains an open question whether the observed greater numerical stability of these SGS HF models holds generally for other types of flows.

2.3. *Relations between different SGS HF models*

In §2.2, we reviewed the classical dynamic SGS HF model (i.e. the EDM), and also proposed three new dynamic SGS HF models (i.e. the GGM, LGGM and QGGM). In this Subsection, we will demonstrate the relationships between the existing and proposed SGS HF models and further show that our proposed GGM, LGGM and QGGM are general modelling approaches, which include a number of previous models as special cases. For convenience, we use table 1 to summarize the SGS HF models to be discussed in this Subsection.

Figure 1, in §1, illustrates the various relationships between the RANS and LES HF models. As shown in this figure, most of the dynamic SGS HF models are unified under the general framework of tensor thermal diffusivity HF modelling originally proposed by Batchelor (cf. (2.8)). Over the past several decades, a significant effort has been made to obtain a physically valid mathematical representation for the tensor thermal diffusivity D_{ij} within the RANS framework (e.g. Daly & Harlow 1970; Yoshizawa 1988; Launder 1988; Rogers, Mansour & Reynolds 1989; Wikström, Wallin & Johansson 2000; Suga & Abe 2000; Park, Sung & Suzuki 2003; So, Jin & Gatski 2004; Younis *et al.* 2005). Among these various approaches for RANS, the simplest and most influential is perhaps the GGDH model of Daly & Harlow (1970), which assumes that D_{ij} is linearly proportional to the Reynolds stress tensor.

As demonstrated previously, a direct implementation of Daly & Harlow's approach in the context of LES results in the GGM, which by analogy assumes D_{ij} to be linearly proportional to the SGS stress tensor τ_{ij} (or its trace-free form τ_{ij}^*). An extension of the GGDH constitutive relation from a homogeneous linear form to an inhomogeneous full linear form results in the proposed LGGM. A further extension of the concept of GGDH from a linear to a quadratic form results in the proposed QGGM, which corresponds to the most general modelling equation for any explicit algebraic constitutive relation that is based on only τ_{ij} and $\partial\bar{\theta}/\partial x_j$ (namely $h_j = f(\tau_{ij}, \partial\bar{\theta}/\partial x_j)$). This general constitutive relation for QGGM is also a direct result of Noll's formula, which is commonly used in continuum physics for constructing constitutive relations for viscoelastic materials and non-Newtonian fluids (Spencer 1971; Zheng 1994).

The derivation of the EDM of Moin *et al.* (1991), DHLTDM of Peng & Davidson (2002), and DFLTDM and DNTDM of Wang *et al.* (2007*b*) as special cases of our general modelling approach (i.e. the QGGM, LGGM and GGM) is straightforward and the hierarchical relations between these models are explicitly illustrated in figure 1. On adoption of the Smagorinsky constitutive relation, the SGS stress tensor assumes the classical form $\tau_{ij}^* = -2C_S\bar{\Delta}^2|\bar{\boldsymbol{S}}|\bar{S}_{ij}$. Substituting this classical SGS stress model into the QGGM and evaluating the SGS time scale as $\mathscr{T} = 1/|\bar{\boldsymbol{S}}|$, results in an equivalent form for the DNTDM of Wang *et al.* (2007*b*):

$$h_j = -D_{jk}^N\frac{\partial\bar{\theta}}{\partial x_k} = -C'_{\theta P}\bar{\Delta}^2|\bar{\boldsymbol{S}}|\frac{\partial\bar{\theta}}{\partial x_j} - C'_{\theta G}\bar{\Delta}^2\bar{S}_{jk}\frac{\partial\bar{\theta}}{\partial x_k} - C'_{\theta Q}\bar{\Delta}^2\frac{\bar{S}_{ji}\bar{S}_{ik}}{|\bar{\boldsymbol{S}}|}\frac{\partial\bar{\theta}}{\partial x_k}. \tag{2.33}$$

Here, $C'_{\theta P}$, $C'_{\theta G}$ and $C'_{\theta Q}$ are model coefficients that can be calibrated dynamically using the vector identity. The tensor diffusivity associated with (2.33) is a quadratic nonlinear tensor function of $\bar{S}_{ij}$ given by

$$D_{jk}^N = C'_{\theta P}\bar{\Delta}^2|\bar{\boldsymbol{S}}|\delta_{jk} + C'_{\theta G}\bar{\Delta}^2\bar{S}_{jk} + C'_{\theta Q}\bar{\Delta}^2\frac{\bar{S}_{ji}\bar{S}_{ik}}{|\bar{\boldsymbol{S}}|}. \tag{2.34}$$

Equation (2.33) represents the most general expression for all the explicit algebraic constitutive relations of the form $h_j = f(\bar{S}_{ij}, \partial\bar{\theta}/\partial x_j)$, which is simply a special case of $h_j = f(\tau_{ij}, \partial\bar{\theta}/\partial x_j)$ when the classical Smagorinsky assumption is used for modelling the SGS stress tensor. As such, we have demonstrated that the DNTDM is a special case of the QGGM.

As in the derivation of (2.33), the DFLTDM and DHLTDM can be directly obtained by substituting the classical Smagorinsky constitutive relation for the SGS stress tensor into the LGGM and GGM, respectively. The DFLTDM of Wang *et al.* (2007*b*) mentioned above assumes the form

$$h_j = -D_{jk}^{FL}\frac{\partial\bar{\theta}}{\partial x_k} = -C'_{\theta P}\bar{\Delta}^2|\bar{\boldsymbol{S}}|\frac{\partial\bar{\theta}}{\partial x_j} - C'_{\theta G}\bar{\Delta}^2\bar{S}_{jk}\frac{\partial\bar{\theta}}{\partial x_k}, \tag{2.35}$$

where the tensor diffusivity is a full linear tensor function of $\bar{S}_{ij}$,

$$D_{jk}^{FL} = f(\bar{S}_{jk}) = C'_{\theta P}\bar{\Delta}^2|\bar{\boldsymbol{S}}|\delta_{jk} + C'_{\theta G}\bar{\Delta}^2\bar{S}_{jk}. \tag{2.36}$$

The DHLTDM of Peng & Davidson (2002) assumes the form

$$h_j = -D_{jk}^{HL}\frac{\partial\bar{\theta}}{\partial x_k} = -C'_{\theta G}\bar{\Delta}^2\bar{S}_{jk}\frac{\partial\bar{\theta}}{\partial x_k}, \tag{2.37}$$

where the tensor diffusivity is a homogeneous linear tensor function of $\bar{S}_{ij}$,

$$D_{jk}^{HL} = f(\bar{S}_{jk}) = C'_{\theta G}\bar{\Delta}^2\bar{S}_{jk}. \tag{2.38}$$

As indicated earlier, the EDM is based on a scalar thermal diffusivity which is spatially isotropic. Assuming that the SGS stress is isotropic (i.e. $\tau_{jk} = -C_1\bar{\Delta}^2|\bar{\boldsymbol{S}}|^2\delta_{jk}$) and evaluating $\mathscr{T}$ using $|\bar{\boldsymbol{S}}|$, the EDM can be directly obtained from the GGM (cf. (2.15)), LGGM (cf. (2.21)), or QGGM (cf. (2.25)).

An alternative method to derive an equivalent form of (2.33) for the DNTDM is to use the GGM (cf. (2.15)). If the SGS time scale is evaluated as $\mathscr{T} = 1/|\bar{\boldsymbol{S}}|$ and the following quadratic model is used for the SGS stress tensor

$$\tau_{jk} = -C_1\bar{\Delta}^2|\bar{\boldsymbol{S}}|^2\delta_{jk} - C_2\bar{\Delta}^2|\bar{\boldsymbol{S}}|\bar{S}_{jk} - C_3\bar{\Delta}^2\bar{S}_{ji}\bar{S}_{ik}, \tag{2.39}$$

then the DNTDM can be directly derived from the GGM. Here, C_1, C_2 and C_3 are model coefficients for the SGS stress tensor. These three coefficients can be incorporated into the coefficients of the SGS HF model, the last of which can then be calibrated dynamically using the vector identity.

The derivation of the EDM, DHLTDM and DFLTDM as special cases of the DNTDM (cf. (2.33)) is straightforward. For example, if $C'_{\theta Q} = 0$, the DNTDM reduces to the DFLTDM. If $C'_{\theta G} = 0$, the DFLTDM further reduces to the EDM. However, if $C'_{\theta P} = 0$, the DFLTDM reduces to the DHLTDM.

Note that although we have demonstrated that the GGM, LGGM and QGGM are specific realizations of a general modelling approach based on the family of constitutive relations $h_j = f(\tau_{ij}, \partial\bar{\theta}/\partial x_j)$, our discussion is restricted to the explicit algebraic approaches for models with a symmetrical tensor thermal diffusivity (i.e. $D_{jk} = D_{kj}$). Consequently, as shown in figure 1, several existing SGS HF models cannot be represented by this proposed approach. For example, SGS HF models that are derived from a non-symmetric tensor thermal diffusivity, designed using the assumption of scale-similarity, extracted using a deconvolution procedure (Stolz, Adams & Kleiser 2001), or constructed using knowledge of the local vortex alignment patterns (Pullin 2000) are not contained within our current modelling approach. As shown in figure 1, these models include the DILTDM (Wang *et al.* 2007*a*), SDMM (Porté-Agel *et al.* 2001*a*,*b*; Kang & Meneveau 2002), DGM, DMM and dynamic scale-similarity SGS HF model (Salvetti & Banerjee 1995). Since these models are not the primary focus of this research, we refer the interested reader to the above mentioned papers for a detailed description of the modelling procedures.

3. Test case and numerical algorithm

In order to validate the proposed SGS HF models, numerical simulations have been performed using two benchmark test cases of fully developed neutrally stratified and unstably stratified turbulent channel flows. For neutrally and unstably stratified turbulent channel flows, the temperature behaves as a passive and an active scalar, respectively. The LES results obtained from the simulations are compared with the DNS data of Kawamura (2007) and Iida & Kasagi (1997), which are available from their websites (henceforth, designated as K-2007 and IK-1997, respectively). Turbulent flows under unstable stratification are of great interest and importance to mechanical engineers, meteorologists and oceanographers. These flows are characterized by the formation of large-scale longitudinal coherent structures, which interact actively with near-wall turbulence. A detailed discussion of the characteristic features of the turbulent thermal flow fields and their concomitant large vortical structures obtained using LES will be provided in §4.

Figure 2 shows the geometry of the computational domain, which has dimensions $L_1 \times L_2 \times L_3 = 5\pi\delta \times 2\delta \times 2\pi\delta$ in the streamwise (x_1), wall-normal (x_2) and spanwise (x_3) directions, respectively. Here, the half-channel width δ is 40 mm. The flow is characterized by a Reynolds number $Re_\tau \overset{\mathrm{def}}{=} u_\tau\delta/\nu = 150$. Here, u_τ represents the wall friction velocity. Table 2 summarizes the sixteen test cases conducted here. Because the momentum and scalar transport processes are coupled, the resolved velocity and

Test case	SGS HF model	SGS stress model	Gr	Grid	Type of scalar
Case 1	EDM	DM	1.3×10^6	$48 \times 32 \times 48$	Active
Case 2A	GGM	DM	1.3×10^6	$48 \times 32 \times 48$	Active
Case 2B		DNM	1.3×10^6	$48 \times 32 \times 48$	Active
Case 2C				$32 \times 24 \times 32$	
Case 2D				$48 \times 32 \times 48$	Passive
Case 2E			4.8×10^6	$48 \times 32 \times 48$	Active
Case 3A	LGGM	DM	1.3×10^6	$48 \times 32 \times 48$	Active
Case 3B		DNM	1.3×10^6	$48 \times 32 \times 48$	Active
Case 3C				$32 \times 24 \times 32$	
Case 3D				$48 \times 32 \times 48$	Passive
Case 3E			4.8×10^6	$48 \times 32 \times 48$	Active
Case 4A	QGGM	DM	1.3×10^6	$48 \times 32 \times 48$	Active
Case 4B		DNM	1.3×10^6	$48 \times 32 \times 48$	Active
Case 4C				$32 \times 24 \times 32$	
Case 4D				$48 \times 32 \times 48$	Passive
Case 4E			4.8×10^6	$48 \times 32 \times 48$	Active

TABLE 2. Summary of 16 test cases for the validation of the GGM, LGGM and QGGM ($Re_\tau = 150$).

temperature fields are influenced by both the SGS stress and HF models. Therefore, in order to evaluate the performance of the proposed GGM, LGGM and QGGM, they are tested with the temperature being treated both as an active and a passive scalar, and are compared with respect to the same SGS stress model (either the DM or DNM). To examine the effects of buoyancy on the heat and fluid flow, two Grashof numbers (i.e. $Gr = 1.3 \times 10^6$ and 4.8×10^6) are tested. The Grashof number is defined as $Gr \overset{\text{def}}{=} g\beta\Delta\theta(2\delta)^3/\nu^2$, where $\Delta\theta = \theta_{wh} - \theta_{wc}$ is the temperature difference between the hot and cold walls.

In order to examine the effect of the grid resolution on the LES results, two coarse grid systems with $48 \times 32 \times 48$ and $32 \times 24 \times 32$ control volumes, have been used to discretize the computational domain. Although both systems are coarse grids, for convenience we will subsequently refer to them as the ‘fine’ and ‘coarse’ grid systems, respectively. Both grid systems are uniform in the streamwise and spanwise directions, and are refined using a hyperbolic-tangent function in the wall-normal direction within the near-wall region. Owing to the dynamic procedure, empirical wall functions are not required for the SGS stress and HF models when they are applied in the near-wall regions.

The governing equations were discretized using a finite volume method. The filtered momentum equations were solved using a fractional-step method. The nonlinear advection term was discretized using a second-order explicit Adams–Bashforth scheme and the viscous diffusion term was discretized using a second-order Crank–Nicolson scheme (Kim & Moin 1985). The pressure correction equation was solved using a multigrid method, and checkerboard oscillations in the pressure field arising from a state of pressure–velocity decoupling on the collocated grid were removed using a nonlinear momentum interpolation scheme (Rhie & Chow 1983). To solve the filtered thermal energy equation, a fourth-order Runge–Kutta method was used to advance the temperature field over a single time step. The time period used to obtain the turbulent flow and temperature statistics was based on 50 000 time steps after the flow became fully developed. In the presentation of the results, quantities non-dimensionalized using the friction velocity u_τ and friction temperature

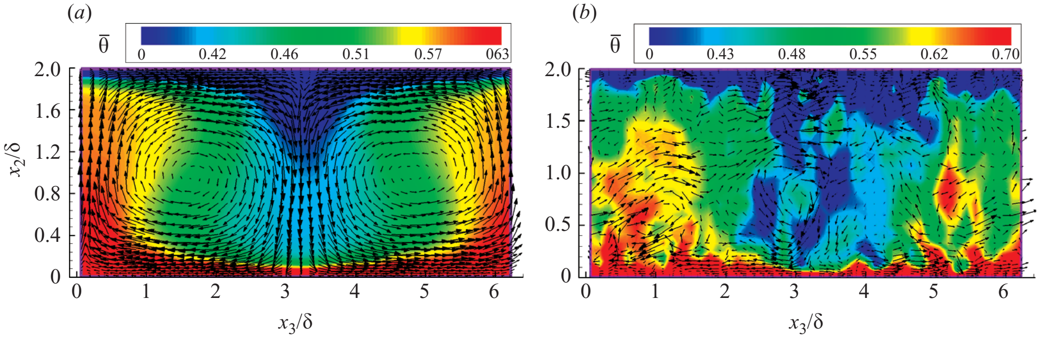

FIGURE 3. Velocity field and isopleths of the resolved temperature field. (x_2, x_3)-view at $x_1/L_1 \approx 0.5$, predicted using GGM and DNM, $Gr = 1.3 \times 10^6$, grid resolution: $48 \times 32 \times 48$, temperature is normalized using the temperature difference between the two walls. (*a*) Time-averaged field, (*b*) instantaneous field.

$\theta_\tau \overset{\text{def}}{=} q_w/(\rho c_P u_\tau)$ are denoted with a superscript +. Here, q_w is the wall heat flux and c_P is the specific heat at constant pressure.

4. Results and analysis

In this Section, we analyse the numerical results obtained using the proposed SGS HF models, in terms of the observed large longitudinal vortex rolls, mean and variance of the temperature and velocity fields, shear stress and heat flux budgets, and forward and backward scatter of local kinetic and scalar energy fluxes between the resolved and subgrid scales.

4.1. *Resolved velocity and temperature fields*

Figures 3(*a*) and 3(*b*) show the time-averaged and instantaneous velocity fields and isopleths of the resolved temperature field in the (x_2, x_3)-plane at the streamwise location $x_1/L_1 \approx 0.5$ for the unstably stratified plane channel flow. These results were predicted using the GGM in conjunction with the DNM. From figure 3(*a*), the time-averaged velocity field exhibits two large symmetrical longitudinal vortex rolls with axes aligned along the streamwise direction. This results in a downdraught in the central region and two updraughts in the peripheral regions. These longitudinal vortex rolls are a consequence of the joint effects of buoyancy and the streamwise pressure gradient, and give rise to a characteristic pattern of organized secondary flow structures that is consistent with the experimental observations of Fukui, Nakagima & Ueda (1991). The large longitudinal vortex rolls have a significant impact on the spatial transport of momentum and thermal energy. Parcels of cold fluid in a layer at the upper wall are entrained into the vortex rolls in the downdraught region, whereas parcels of hot fluid in a layer at the lower wall are entrained into the vortex rolls in the updraught regions resulting in the vigorous mixing of hot and cold fluid parcels. In contrast to the time-averaged fields, the instantaneous velocity and thermal fields displayed in figure 3(*b*) show ejections and sweeps of irregular large flow structures (as marked by the various temperature isopleths) between the near-wall and outer flow regions.

In order to determine if the proposed SGS HF models are sensitive to the existence of buoyancy, temperature is treated both as an active and a passive scalar in the tests.

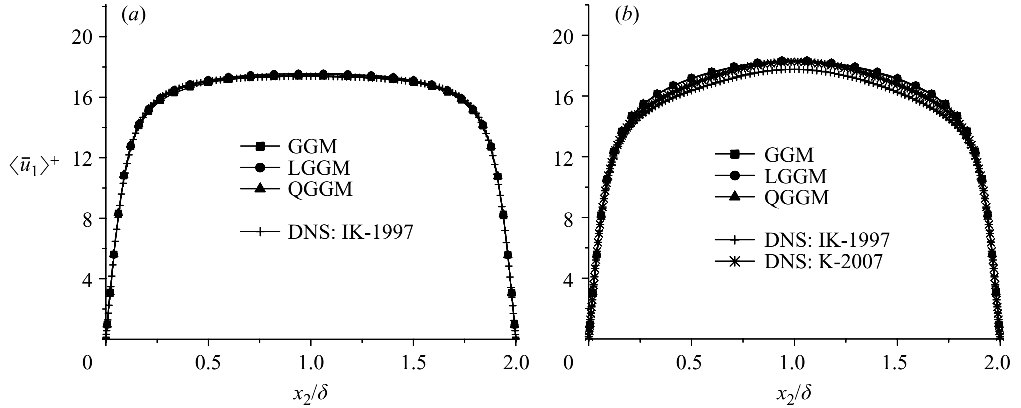

FIGURE 4. Velocity profiles predicted using three proposed SGS HF models with temperature treated as an active or a passive scalar (SGS stress model: DNM; $Gr = 1.3 \times 10^6$; grid resolution: $48 \times 32 \times 48$). K-2007: DNS dataset for neutrally stratified flow; IK-1997: DNS data for both passive and active scalars. (*a*) Active scalar, (*b*) passive scalar.

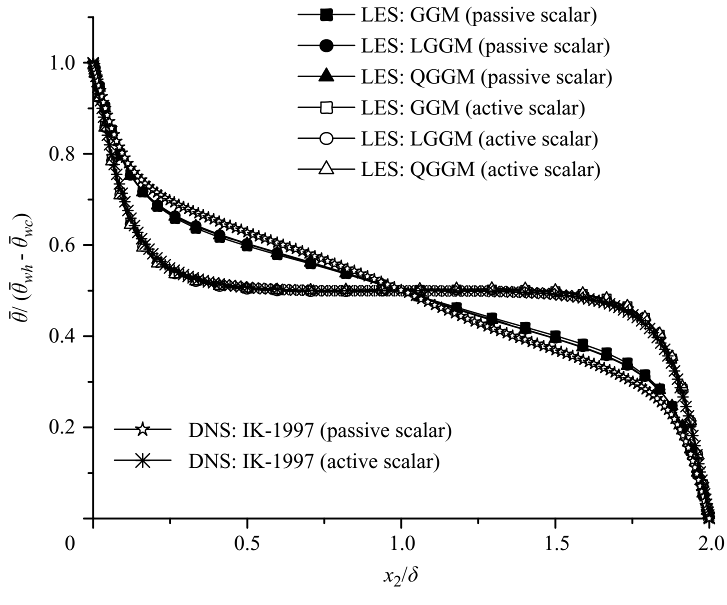

FIGURE 5. Comparison of the temperature profiles predicted using three proposed SGS HF models with the temperature treated as an active or a passive scalar (SGS stress model: DNM; $Gr = 1.3 \times 10^6$; grid resolution: $48 \times 32 \times 48$).

For the active scalar test cases, the temperature and velocity fields are coupled and the buoyant force contributes to the momentum transport process. However, for the passive scalar test cases, the buoyancy term is absent from the momentum equation (cf. (2.2)), and consequently, the velocity field is decoupled from the temperature field and the flow becomes neutrally stratified. From figures 4(*a*), 4(*b*) and 5, it is seen that for both the active and passive scalar test cases, the model predictions of the time- and plane-averaged streamwise velocity and temperature profiles conform well with the reported DNS data of Kawamura (2007) and Iida & Kasagi (1997). The

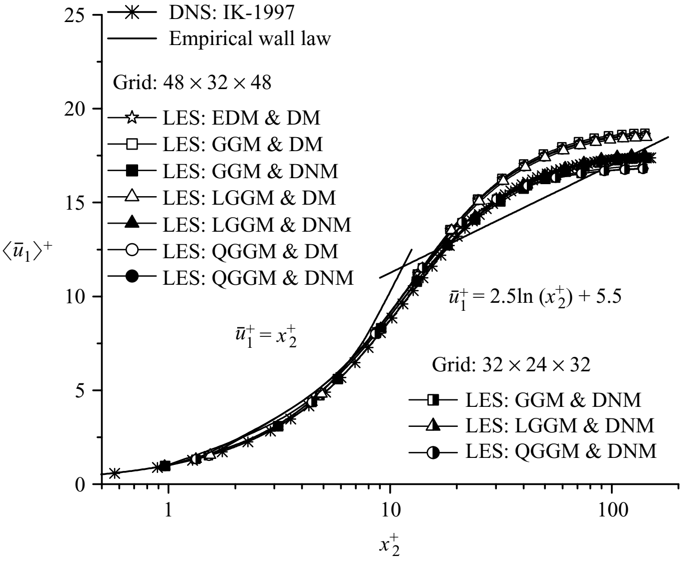

FIGURE 6. Mean profiles of the resolved streamwise velocity ($Gr = 1.3 \times 10^6$).

large organized longitudinal vortex rolls as shown in figure 3 are characteristic of an unstably stratified channel flow for which the temperature functions as an active scalar. These large longitudinal vortex rolls have a significant impact on both the predicted velocity and temperature profiles. As shown in figures 4 and 5, owing to the existence of these vortex rolls, the momentum and thermal boundary layers evolve much faster in the active scalar case than in the passive scalar case. Correspondingly, for the active scalar case, the flow field is more turbulent and the turbulent diffusion of the scalar (temperature) is more effective in the wall-normal direction.

Figure 6 shows the mean resolved streamwise velocity profiles (i.e. $\langle \bar{u}_1 \rangle$) predicted by the three proposed SGS HF models for the benchmark test case of $Gr = 1.3 \times 10^6$ using two grid systems. These velocity profiles are compared with those obtained using the conventional EDM and with DNS data of Iida & Kasagi (1997). The empirical law of the wall for a neutrally stratified flow is also displayed for reference purposes. As evident from figures 4 and 5, because the time- and plane-averaged streamwise velocity and temperature profiles are symmetrical in the wall-normal direction, we only show one-half of the complete velocity profiles using the wall coordinates in the hot-wall region. For a given fixed grid system, the predicted values of the wall friction velocity u_τ and temperature θ_τ vary slightly between the different SGS modelling approaches. Therefore, the profiles of a physical quantity (e.g. the mean velocity, temperature and turbulent intensities) predicted using different SGS models, when displayed using the wall coordinates, are expected to be different, which reflects the differences in the predictive accuracy of the SGS HF models in the near-wall region. As shown in figure 6, owing to the existence of the buoyancy, the predicted mean velocity profiles deviate from the familiar log law. A comparison of the ten different SGS model combinations tested suggests that the predictions of $\langle \bar{u}_1 \rangle$ obtained using the DNM conform better with the DNS data than predictions obtained using the DM. Interestingly, the coarse grid prediction based on the DNM is even better than the fine grid prediction based on the DM.

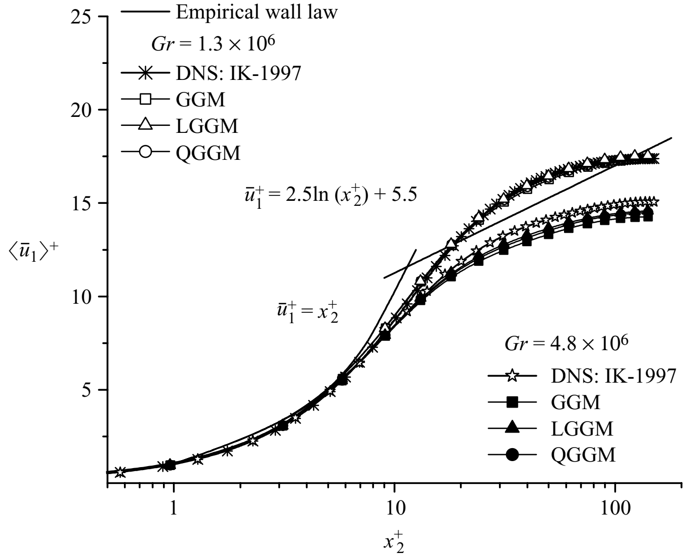

FIGURE 7. Effect of Grashof number on the mean resolved streamwise velocity profile (SGS stress model: DNM; grid resolution: 48 × 32 × 48).

Figure 7 demonstrates the effects of buoyancy on the resolved velocity profile predicted using the three proposed SGS HF models (in conjunction with the DNM). From figure 7, it is seen that the performance of the GGM, LGGM and QGGM is similar at the two different Grashof numbers. As Grashof number increases, the non-dimensionalized streamwise velocity shifts downwards in response to the increase in the buoyancy, which is consistent with the observation of Iida & Kasagi (1997).

Figure 8 compares the predicted resolved turbulence intensities (or root-mean-square (RMS) values, which are defined as $\bar{u}_{i,rms}^+ \overset{\text{def}}{=} \langle ((\bar{u}_i - \langle \bar{u}_i \rangle)/u_\tau)^2 \rangle^{1/2}$ for $i = 1$, 2 and 3) with the DNS data. As for the case of the mean resolved streamwise velocity profiles, under exactly the same test condition, the predictions of $\bar{u}_{i,rms}$ using the DNM are generally in better agreement with the DNS data than those obtained using the DM, especially in terms of the streamwise component. Because resolved turbulence intensities are important physical quantities and of great interest to researchers, it is popular in the literature to compare directly the values of turbulence intensities obtained from LES and DNS approaches, especially when different LES test cases are investigated under the same test condition. However, as pointed out by Winckelmans, Jeanmart & Carati (2002), one should expect to observe differences in the predicted values of the turbulence intensities obtained from LES and DNS, owing to the fact that conventional LES provides only a model for the trace-free SGS stress tensor (namely the information embodied in the diagonal components τ_{ii} (no summation on the repeated subscript) of the SGS stress tensor is not available). For a conventional LES approach, the prediction of the normal components of the Reynolds stress tensor (turbulence intensities) is influenced by the modelled SGS stresses and the grid resolution used. To demonstrate this, we compare in figure 9 the prediction of the resolved streamwise turbulent intensity $\bar{u}_{1,rms}^+$ based on two different grid resolutions. As expected, for all the three tested SGS HF models, the prediction of $\bar{u}_{1,rms}^+$ based on the coarser grid is less satisfactory in comparison with the DNS results, demonstrating the effects of the grid resolution on the LES prediction of resolved

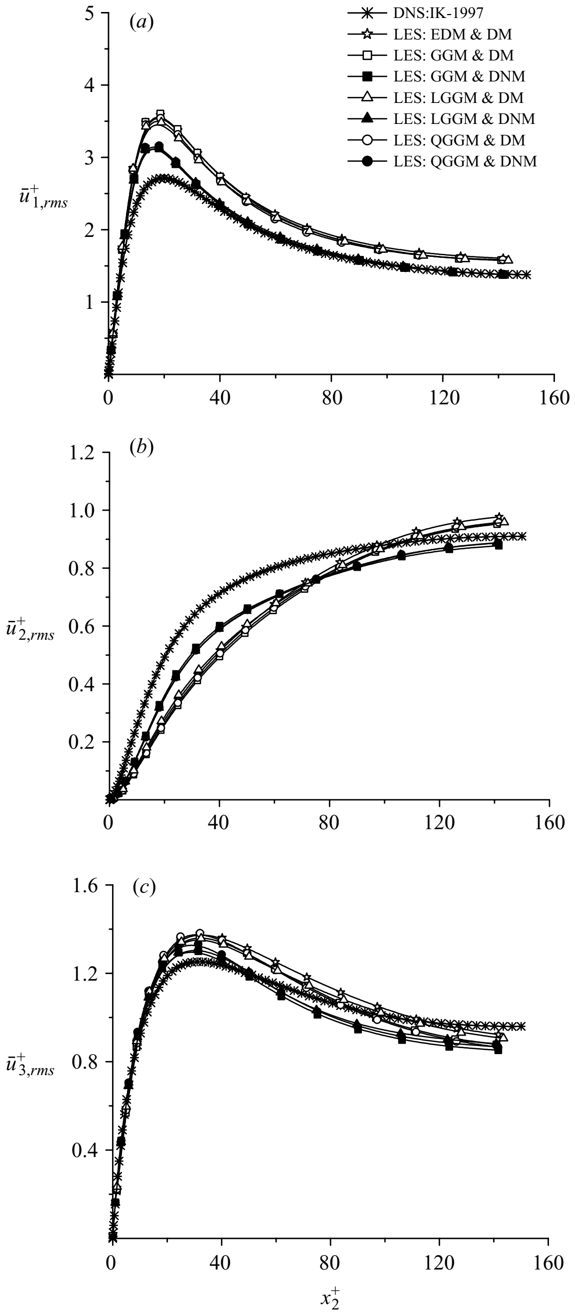

FIGURE 8. Resolved turbulence intensities ($Gr = 1.3 \times 10^6$; grid resolution: $48 \times 32 \times 48$). (*a*) Streamwise component, (*b*) wall-normal component, (*c*) spanwise component.

turbulent intensities. Figure 9 also shows the results for LES without SGS stress and HF models for both grid systems. As expected, the predictions from LES without SGS models are poorer in comparison to those obtained with SGS models at both the coarse and fine grid resolutions, indicating that the SGS models utilized in the simulations are properly capturing (approximately or better) the physics associated

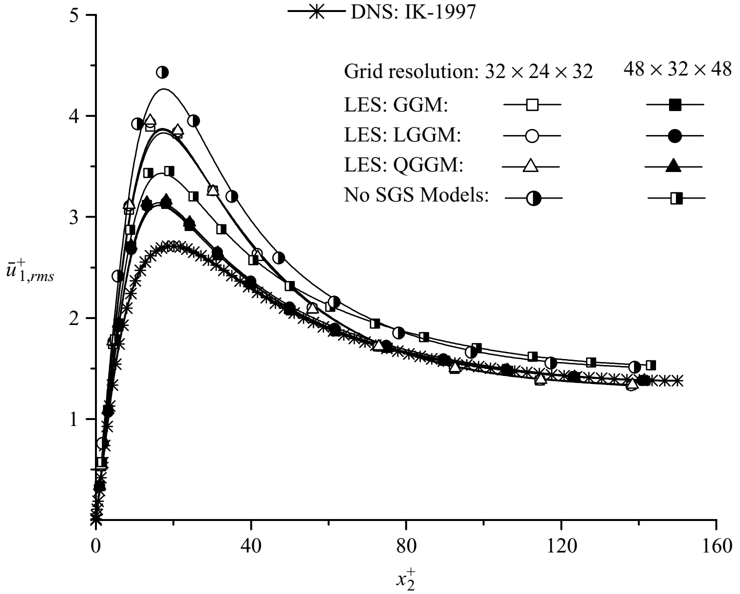

FIGURE 9. Resolved streamwise turbulent intensity predicted using two different grid resolutions (SGS stress model: DNM; $Gr = 1.3 \times 10^6$).

with subgrid-scale motions of the flow. This is consistent with the observation of Ghosal & Rogers (1997), who studied a turbulent plane wake flow using LES with and without SGS stress models.

However, it should be indicated here that although the method of LES without SGS models is useful in demonstrating the SGS effects in a qualitative manner, it is an unphysical simulation in the context of a conventional LES (in contrast to the approach of a monotonically integrated large eddy simulation (MILES) which does not rely on explicit SGS modelling (Fureby & Grinstein 1999)). Given the coarse resolutions used in LES, the method of LES without SGS models is neither an LES nor a DNS (because DNS requires the finest turbulent motions at the Kolmogorov scale to be resolved, temporally and spatially, and LES necessarily gives rise to SGS stresses which cannot generally be ignored). As a consequence, there is no strict justification that the results obtained from the conventional LES without SGS models necessarily represent realistic turbulence that can be unambiguously compared with turbulence data obtained from experiments or DNS. Furthermore, as noted by Vreman (2004), LES without SGS models can be numerically unstable because it is possible for TKE to gradually pile up at the high-wavenumber cutoff without an SGS stress model, eventually leading to numerical instability or even divergence in the simulations.

Figure 10 compares the profiles of the mean resolved temperature predicted by the different SGS models based on two grid systems. Although slight differences exist, the LES predictions are generally consistent with the DNS result. Owing to the effect of buoyancy, the mean temperature profile deviates from the conventional law-of-the-wall relationship. Of the ten test cases shown in the figure, predictions obtained using the various SGS HF models in conjunction with the DM all slightly overpredict the temperature in comparison with the DNS data. Figure 11 displays the effects of buoyancy on the resolved temperature distribution. The predictive performances of

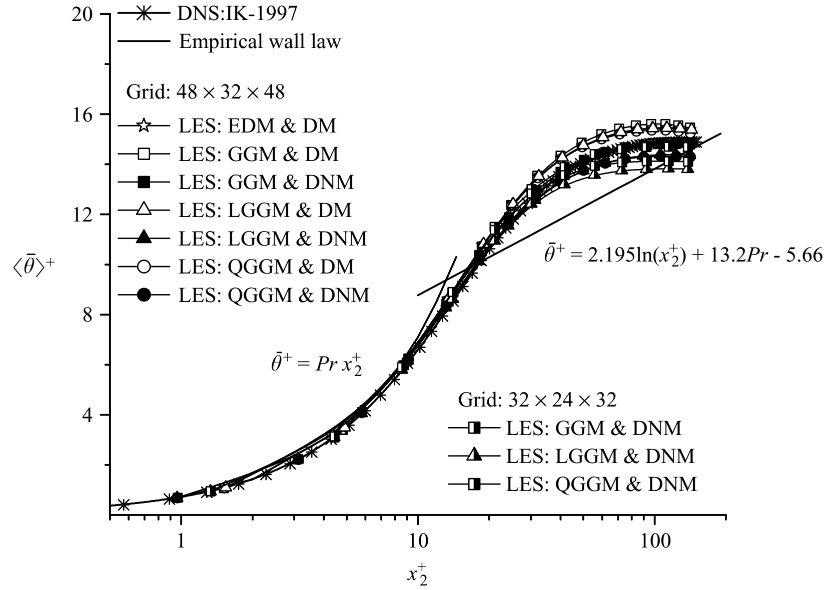

FIGURE 10. Mean profiles of the resolved temperature ($Gr = 1.3 \times 10^6$).

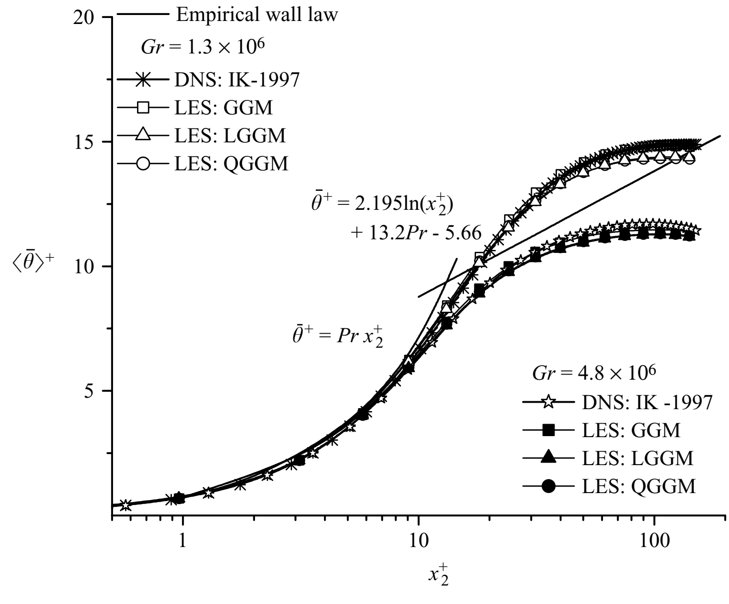

FIGURE 11. Effect of Grashof number on the mean resolved temperature profile (SGS stress model: DNM; grid resolution: 48 × 32 × 48).

the GGM, LGGM and QGGM are, in general, similar for the two tested Grashof numbers. By comparing figures 7 and 11, it is observed that for an unstably stratified turbulent channel flow, the effect of buoyancy on the mean temperature profile is analogous to that on the mean velocity profile. As the Grashof number increases from 1.3×10^6 to 4.8×10^6, the non-dimensionalized temperature profiles shift downwards

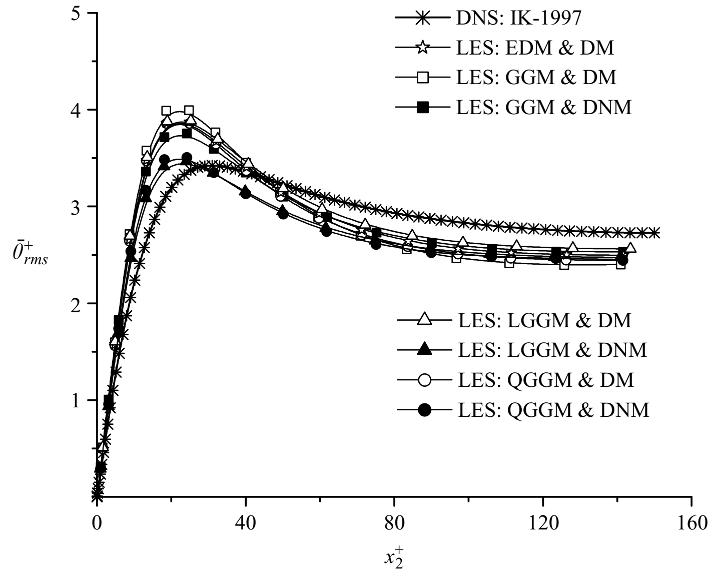

FIGURE 12. Profiles of the root-mean-square of the resolved temperature fluctuations ($Gr = 1.3 \times 10^6$; grid resolution: 48 × 32 × 48).

due to an increased buoyancy and increases in the values of the wall heat flux and wall friction temperature (on noting that $\langle \bar{\theta} \rangle^+ = \langle \bar{\theta} \rangle / \theta_\tau$ with $\theta_\tau \overset{\text{def}}{=} q_w/(\rho c_P u_\tau)$).

Figure 12 displays the resolved temperature fluctuation (RMS of $\bar{\theta}$): $\bar{\theta}^+_{rms} \overset{\text{def}}{=} \langle ((\bar{\theta} - \langle \bar{\theta} \rangle)/\theta_\tau)^2 \rangle^{1/2}$. In conformance with previous observations, when compared with the DNS data, the combinations of SGS HF models with the DNM generally provide better predictions of the RMS temperature fluctuations than those with the DM, especially in the buffer layer. This indicates that for LES of scalar (thermal energy) transport, it is beneficial to use an advanced SGS stress model (such as the DNM) in the filtered momentum equation to obtain a more accurate velocity field, because this leads subsequently to an improved prediction of the scalar (temperature) field. This conclusion is not surprising because for both active and passive scalars, the resolved velocity field plays a critical role in the scalar dispersion through the advection term appearing in (2.3). From figure 12, it is also observed that predictions obtained using the LGGM and QGGM are in better agreement with the DNS data than those obtained using the GGM (when they are tested in conjunction with the DNM), especially in the buffer layer. It should be noted that there are two types of SGS models involved in LES of thermal flows; namely, the SGS stress and HF models. For the test case adopted, resolved flow field quantities such as the turbulent velocity intensities are more sensitive to the SGS stress models (the effect of SGS stress modelling is evident in figure 8). In contrast, resolved temperature field quantities such as the RMS temperature fluctuations are more sensitive to the SGS HF model (the effect of SGS HF modelling is evident in figure 12).

4.2. *Budgets of shear stresses and heat fluxes*

In order to investigate the performance of our proposed GGM, LGGM and QGGM in terms of the momentum and thermal energy balances, we examined the budgets of the shear stresses and heat fluxes across the channel. For LES of a channel flow, an instantaneous filtered quantity can be decomposed into a time- and plane-averaged

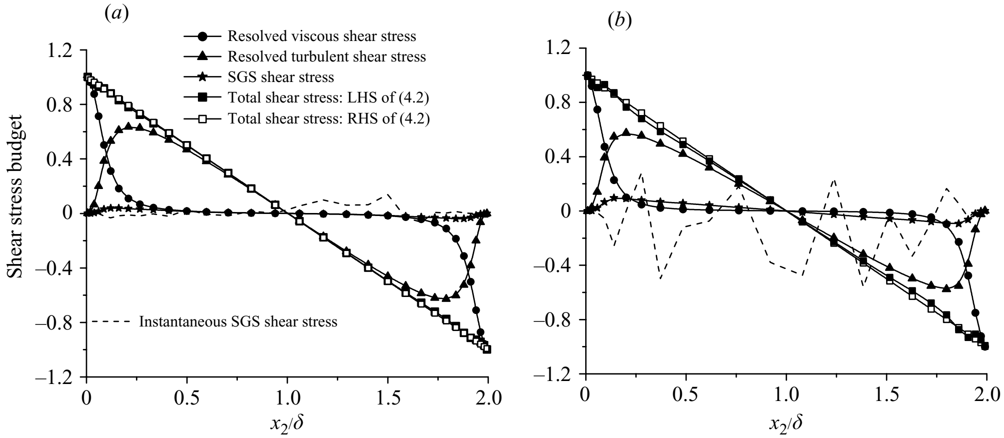

FIGURE 13. Budget of non-dimensionalized wall-normal shear stresses at different grid resolutions (*a*) 48 × 32 × 48, (*b*) 32 × 24 × 32 (SGS stress model: DNM; SGS HF model: LGGM; $Gr = 1.3 \times 10^6$; location for the instantaneous SGS shear stress distribution is: $x_1/L_1 = x_3/L_3 \approx 0.5$).

component and a residual component as

$$\bar{\phi} = \langle \bar{\phi} \rangle + \bar{\phi}''. \tag{4.1}$$

On assuming that the flow is statistically stationary and homogeneous in the (x_1, x_3)-plane, an equation that balances the time- and plane-averaged shear stresses at an arbitrary wall-normal location x_2 is obtained by substituting (4.1) into the filtered streamwise momentum equation and then integrating the resulting equation from 0 to x_2 in the wall-normal direction to give

$$\nu \frac{\partial \langle \bar{u}_1 \rangle}{\partial x_2} - \langle \bar{u}_1'' \bar{u}_2'' \rangle - \langle \tau_{12} \rangle = -\frac{1}{\rho} \frac{\partial \langle \bar{p} \rangle}{\partial x_1} x_2 + \frac{\tau_{wh}}{\rho}. \tag{4.2}$$

The three terms on the left-hand side of (4.2) represent the resolved viscous shear stress, resolved turbulent shear stress, and SGS shear stress, respectively. The two terms on the right-hand side of the equation represent the resolved integrated shear force due to the mean pressure gradient, and the resolved viscous shear stress at the hot wall ($\tau_{wh} = \rho\nu(\partial\langle \bar{u}_1 \rangle/\partial x_2)|_{x_2=0}$), respectively.

Figures 13(*a*) and 13(*b*) show the shear stress budget predicted using the DNM and LGGM at two different grid resolutions. All the terms shown in the figures are non-dimensionalized using the wall shear stress term (i.e. $\tau_w/\rho = u_\tau^2$). Although two assumptions were used in the derivation of (4.2) from the filtered momentum equation, the balance expressed by this equation is consistent with the results obtained from the numerical simulation. As evident in both figures 13(*a*) and 13(*b*), the total shear stress calculated from the left-hand side of (4.2) agrees very well with that calculated from the right-hand side of the equation at both grid resolutions. In general, the magnitude of the time- and plane-averaged SGS shear stress component $\langle -\tau_{12} \rangle$ is smaller than those of the other shear stress components. However, as shown in figures 13(*a*) and 13(*b*), the instantaneous value of the SGS shear stress $-\tau_{12}$ (shown using the dashed line) can be significant at a specific location (e.g. at points along the vertical line determined by the intersection of the two planes at $x_1/L_1 \approx 0.5$ and $x_3/L_3 \approx 0.5$). By comparing figures 13(*a*) and 13(*b*), it is seen that both the instantaneous and time- and plane-averaged SGS shear stress components become larger as the grid

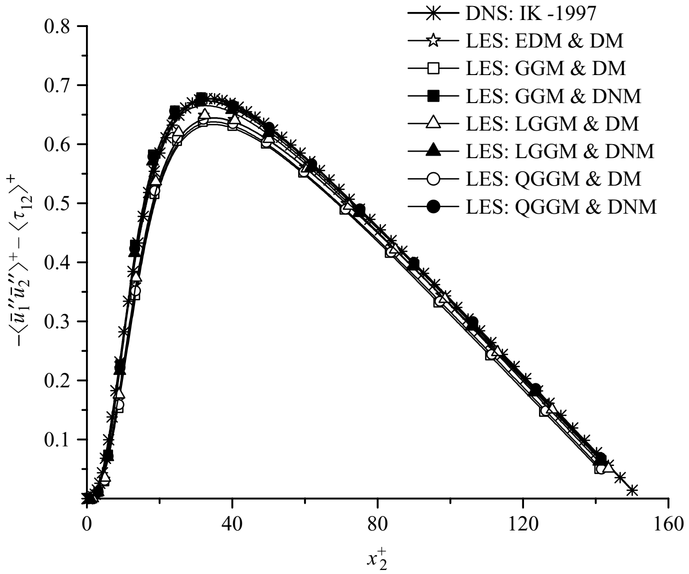

FIGURE 14. Predicted Reynolds shear stress displayed using wall coordinates ($Gr = 1.3 \times 10^6$; grid resolution: 48 × 32 × 48).

resolution becomes coarser. As for the case of the LGGM, the GGM and QGGM also successfully predicted the shear stress budget (not shown) at the two different grid resolutions used here.

As demonstrated by Winckelmans *et al.* (2002) (see also Sagaut 2002), the time- and plane-averaged deviatoric part of the 'true' (or exact) Reynolds stresses (denoted using $\langle u_i'^e u_j'^e\rangle$) obtained from a DNS approach can be estimated by LES using the resolved turbulent and SGS stresses, i.e. $\langle u_i'^e u_j'^e\rangle \approx \langle\bar{u}_i''\bar{u}_j''\rangle + \langle\tau_{ij}\rangle$. Figure 14 compares the Reynolds shear stresses (i.e. $-\langle\bar{u}_1''\bar{u}_2''\rangle^+ - \langle\tau_{12}\rangle^+$) predicted using three SGS HF models (in conjunction with the DM and DNM) with the DNS results (i.e. $-\langle u_1'^e u_2'^e\rangle^+$). Consistent with our previous observations, use of the DNM for modelling the SGS stress tensor gives predictions of the resolved turbulent shear stress that conform better with the DNS data. Figures 15(*a*) and 15(*b*) show the budget the Reynolds stresses (predicted using the DNM and LGGM) in comparison with the DNS data of the hot-wall region at two different grid resolutions. As the grid resolution becomes coarser, the SGS effects of course become more significant. As shown in the figure 15, the SGS shear stress component contributes considerably to the total budget of the predicted Reynolds stress. The maximum value of the ratio between the time- and plane-averaged SGS and total Reynolds shear stresses (i.e. $-\langle\tau_{12}\rangle/(-\langle\bar{u}_1''\bar{u}_2''\rangle - \langle\tau_{12}\rangle)$), is 7.4% and 14.9% for the fine and coarse grid systems, respectively.

Following a procedure similar to that used for deriving (4.2), the time- and plane-averaged equation expressing the balance in the mean wall-normal heat fluxes at any arbitrary wall-normal location x_2 can be obtained from the filtered energy equation (2.3):

$$-\alpha\frac{\partial\langle\bar{\theta}\rangle}{\partial x_2} + \langle\bar{u}_2''\bar{\theta}''\rangle + \langle h_2\rangle = \frac{q_{wh}}{\rho c_P}, \tag{4.3}$$

where $q_{wh} \overset{\text{def}}{=} -\lambda(\partial\langle\bar{\theta}\rangle/\partial x_2)\,|_{x_2=0}$ is the resolved molecular heat flux at the hot wall, and λ is the thermal conductivity. The three wall-normal HF components on the left-hand

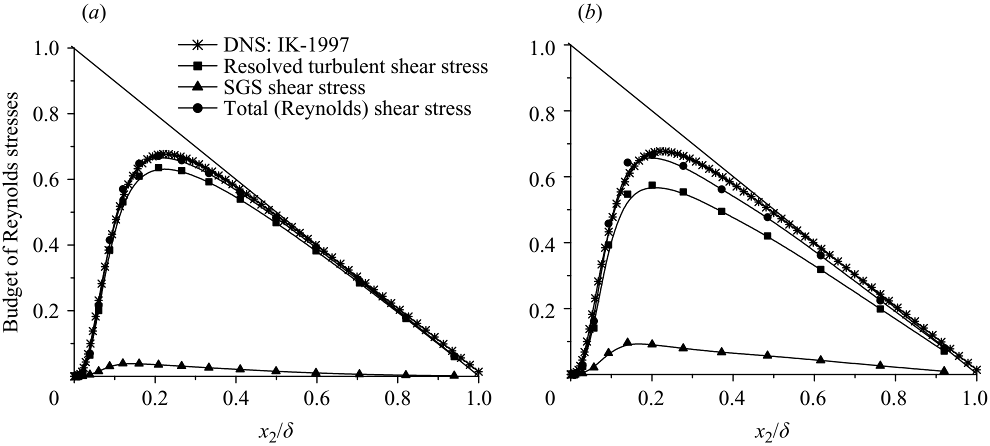

FIGURE 15. Budget of the predicted Reynolds shear stresses in the hot wall region at different grid resolutions (*a*) 48 × 32 × 48, (*b*) 32 × 24 × 32 (SGS stress model: DNM; SGS HF model: LGGM; $Gr = 1.3 \times 10^6$). Resolved turbulent shear stress: $-\langle \bar{u}_1''\bar{u}_2''\rangle^+$, SGS stress: $-\langle \tau_{12}\rangle^+$, total (Reynolds) shear stress: $-\langle \bar{u}_1''\bar{u}_2''\rangle^+ - \langle \tau_{12}\rangle^+$.

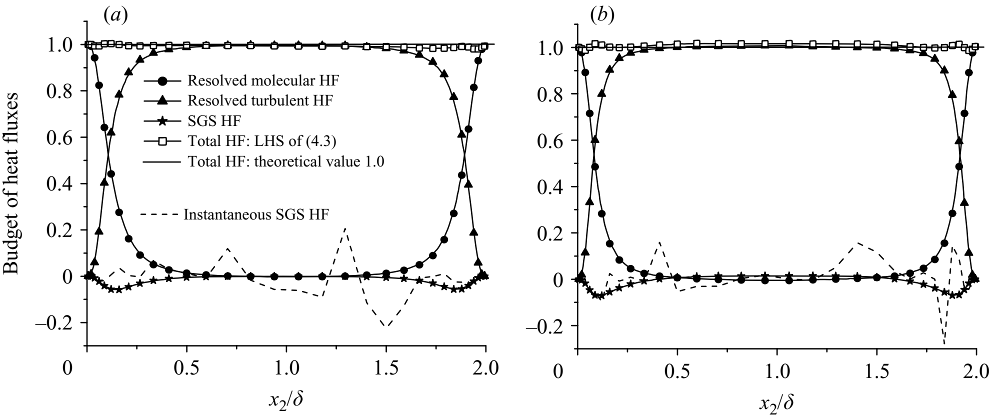

FIGURE 16. Budget of non-dimensionalized wall-normal heat fluxes for different Grashof numbers; (*a*) 1.3×10^6, (*b*) 4.8×10^6 (SGS stress model: DNM; SGS HF model: GGM; grid resolution: 48 × 32 × 48; location for the instantaneous SGS shear stress distribution is: $x_1/L_1 = x_3/L_3 \approx 0.5$).

side of (4.3) correspond to the resolved molecular heat flux, resolved turbulent heat flux, and SGS heat flux, respectively. Figure 16 displays the budget of the wall-normal heat flux terms predicted by the GGM (in conjunction with the SGS stress model DNM) for two different Grashof numbers. All the terms shown in the figure are non-dimensionalized by the molecular heat flux at the hot wall, i.e. $q_{wh}/\rho c_p = u_{\tau h}\theta_{\tau h}$. With this special normalization, the total heat flux given by the right-hand side of (4.3) becomes unity. As shown in figures 16(*a*) and 16(*b*), the GGM provides a good balance of the wall-normal heat fluxes at both Grashof numbers, since it is evident from these figures that the total heat flux calculated from the left-hand side of (4.3) agrees well with the theoretical value of 1.0. Figures 16(*a*) and 16(*b*) also show that the instantaneous values of the wall-normal SGS HF h_2 can fluctuate locally with

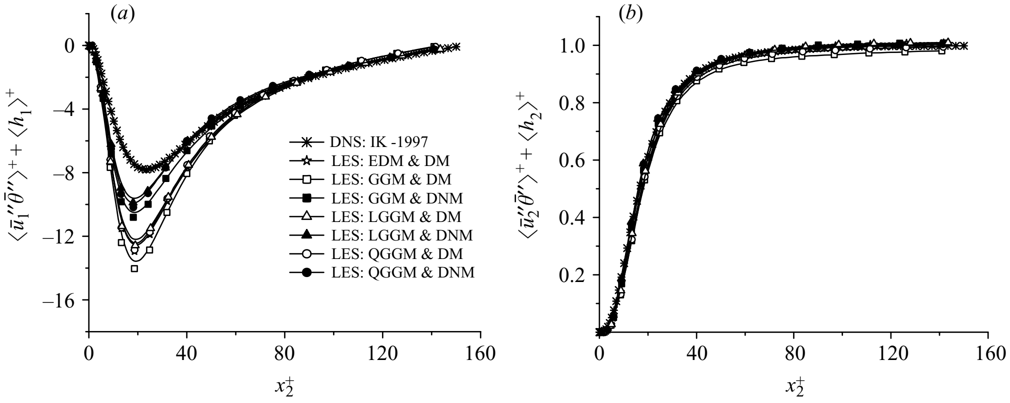

FIGURE 17. Total turbulent heat fluxes displayed using wall coordinates ($Gr = 1.3 \times 10^6$; grid resolution: $48 \times 32 \times 48$). (*a*) Streamwise component, (*b*) wall-normal component.

a relatively large amplitude (e.g. at points along the vertical line determined by the intersection of two planes at $x_1/L_1 \approx 0.5$ and $x_3/L_3 \approx 0.5$, shown using a dashed line) in contrast to the time- and plane-averaged values $\langle h_2\rangle$. As in the case of the GGM exhibited in figures 16(*a*) and 16(*b*), the LGGM and QGGM also successfully predicted the heat flux budget (not shown) at both Grashof numbers.

The time- and plane-averaged value of the 'true' (or exact) turbulent heat flux (denoted by $\langle u_j'^e\theta'^e\rangle$) obtained from a DNS approach can be estimated by LES using the resolved turbulent and SGS heat fluxes, i.e. $\langle u_j'^e\theta'^e\rangle \approx \langle \bar{u}_j''\bar{\theta}''\rangle + \langle h_j\rangle$. Figures 17(*a*) and 17(*b*) show the total streamwise and total wall-normal turbulent heat fluxes (i.e. $\langle \bar{u}_1''\bar{\theta}''\rangle^+ + \langle h_1\rangle^+$ and $\langle \bar{u}_2''\bar{\theta}''\rangle^+ + \langle h_2\rangle^+$, respectively) using wall coordinates in comparison with the DNS results (i.e. $\langle u_1'^e\theta'^e\rangle^+$ and $\langle u_2'^e\theta'^e\rangle^+$, respectively). Although the performance of the seven SGS model combinations is very similar in terms of their predictions of the wall-normal turbulent HF component (cf. figure 17(*b*), all of which are in good agreement with the DNS results), distinct differences exist between their predictions of the streamwise turbulent HF component (cf. figure 17*a*). Once again, it is observed that use of the DNM gives predictions of the total streamwise turbulent HF that are in better agreement with the DNS data. Furthermore, figure 17(*a*) shows that for the three proposed models, use of the LGGM and QGGM for modelling the SGS HF yields predictions of the total streamwise HF that conform slightly better with the DNS data than that provided by the GGM (in the context of using the DNM for modelling of the SGS stresses, shown using the solid symbols in figure 17*a*).

4.3. *SGS effects on local kinetic and scalar energy fluxes*

In the previous Subsection, we have examined the basic physical features of the instantaneous and time- and plane-averaged velocity and temperature fields at both the resolved and subgrid scale levels. In this Subsection, we investigate the local kinetic energy (KE) and scalar energy (SE) transfer between the resolved and subgrid scales, which characterizes the physical interaction between these two scales of motions and also reflects the SGS effects related to the SGS stress and HF models.

4.3.1. *SGS effects on the budget of the kinetic energy of the filtered flow*

The filtered kinetic energy (defined as $\overline{E} \overset{\text{def}}{=} \frac{1}{2}\overline{u_i u_i}$) of the flow can be decomposed as

$$\overline{E} = k_r + k_{sgs}, \tag{4.4}$$

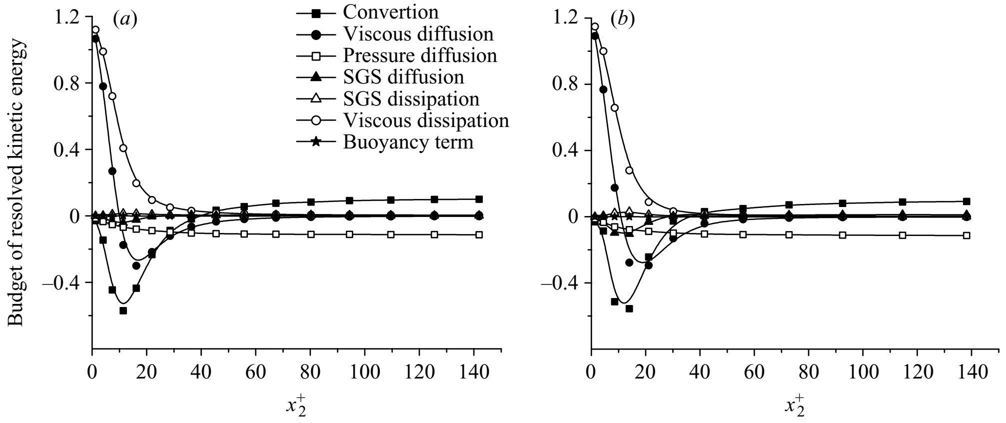

FIGURE 18. Budget of the time- and plane-averaged resolved KE $\langle k_r \rangle$ of the resolved velocity field in the wall-normal direction at different grid resolutions (*a*) 48 × 32 × 48, (*b*) 32 × 24 × 32 (SGS stress model: DNM; SGS HF model: LGGM; $Gr = 1.3 \times 10^6$). Convection: $\langle Con \rangle = \frac{\partial}{\partial x_2} \langle \bar{u}_2 k_r \rangle$; viscous diffusion: $\langle D_{vis} \rangle = \frac{\partial}{\partial x_2} \langle 2\nu \bar{S}_{i2} \bar{u}_i \rangle$; pressure diffusion: $\langle D_{pres} \rangle = \frac{1}{\rho} \langle \bar{u}_j \frac{\partial \bar{p}}{\partial x_j} \rangle$; SGS diffusion: $\langle D_{sgs} \rangle = \frac{\partial}{\partial x_2} \langle \tau_{i2}^* \bar{u}_i \rangle$; SGS dissipation: $\langle P_r \rangle = \langle -\tau_{ij}^* \bar{S}_{ij} \rangle$; viscous dissipation: $\langle \varepsilon_r \rangle = \langle 2\nu \bar{S}_{ij} \bar{S}_{ij} \rangle$; buoyancy term: $\langle B_r \rangle = \langle -\beta g \bar{u}_2 (\bar{\theta} - \Theta_r) \rangle$. All quantities shown in the figures are non-dimensionalized using a constant wall dissipation rate: $\varepsilon'_{wall} = u_\tau^4/\nu$.

where $k_r \overset{\text{def}}{=} \frac{1}{2}\bar{u}_i\bar{u}_i$ is the resolved KE of the resolved (or filtered) velocity field, and $k_{sgs} \overset{\text{def}}{=} \frac{1}{2}\tau_{ii} = \frac{1}{2}(\overline{u_i u_i} - \bar{u}_i\bar{u}_i)$ is the SGS KE. Following Pope (2000), it can be shown that the transport equation for k_r takes the following form in the context of an incompressible thermal flow:

$$\frac{\mathrm{D}k_r}{\mathrm{D}t} = \frac{\partial(F_{ij}\bar{u}_i)}{\partial x_j} - \varepsilon_r - P_r - B_r, \tag{4.5}$$

where

$$\frac{\mathrm{D}(\cdot)}{\mathrm{D}t} \overset{\text{def}}{=} \frac{\partial(\cdot)}{\partial t} + \bar{u}_j \frac{\partial(\cdot)}{\partial x_j}$$

represents the material derivative of a variable, $F_{ij} \overset{\text{def}}{=} 2\nu\bar{S}_{ij} - \tau_{ij}^* - (\bar{p}/\rho)\delta_{ij}$ is the stress term, $\varepsilon_r \overset{\text{def}}{=} 2\nu\bar{S}_{ij}\bar{S}_{ij}$, $P_r \overset{\text{def}}{=} -\tau_{ij}^*\bar{S}_{ij}$ and $B_r \overset{\text{def}}{=} \beta g_i \bar{u}_i (\bar{\theta} - \Theta_r)$. The four terms on the right-hand side of (4.5) represent the rates of the stress diffusion, resolved viscous dissipation, SGS dissipation and buoyancy production/suppression (depending on its sign) of the resolved KE k_r, respectively.

Assuming that the flow field is steady and homogeneous in the (x_1, x_3)-plane, the following equation can be derived from (4.5), which breaks down the budget of the time- and plane-averaged $\langle k_r \rangle$ in the wall-normal (x_2) direction:

$$\langle Con \rangle = \langle D_{vis} \rangle - \langle D_{sgs} \rangle - \langle D_{pres} \rangle - \langle \varepsilon_r \rangle - \langle P_r \rangle - \langle B_r \rangle, \tag{4.6}$$

where $\langle Con \rangle \overset{\text{def}}{=} (\partial/\partial x_2)\langle \bar{u}_2 k_r \rangle$ is the averaged resolved convection term, $\langle D_{vis} \rangle \overset{\text{def}}{=} (\partial/\partial x_2)\langle 2\nu\bar{S}_{i2}\bar{u}_i \rangle$ is the averaged resolved viscous diffusion term, $\langle D_{sgs} \rangle \overset{\text{def}}{=} (\partial/\partial x_2)\langle \tau_{i2}^*\bar{u}_i \rangle$ is the averaged SGS diffusion term, $\langle D_{pres} \rangle \overset{\text{def}}{=} (1/\rho)\langle \bar{u}_j(\partial\bar{p}/\partial x_j) \rangle$ is the averaged resolved pressure diffusion term, and $\langle \varepsilon_r \rangle$, $\langle P_r \rangle$ and $\langle B_r \rangle$ are the averaged resolved viscous dissipation, SGS dissipation and averaged resolved buoyancy production/suppression terms, respectively. Figures 18(*a*) and 18(*b*) show the budget of $\langle k_r \rangle$ predicted using the DNM and LGGM at two different grid resolutions. Both

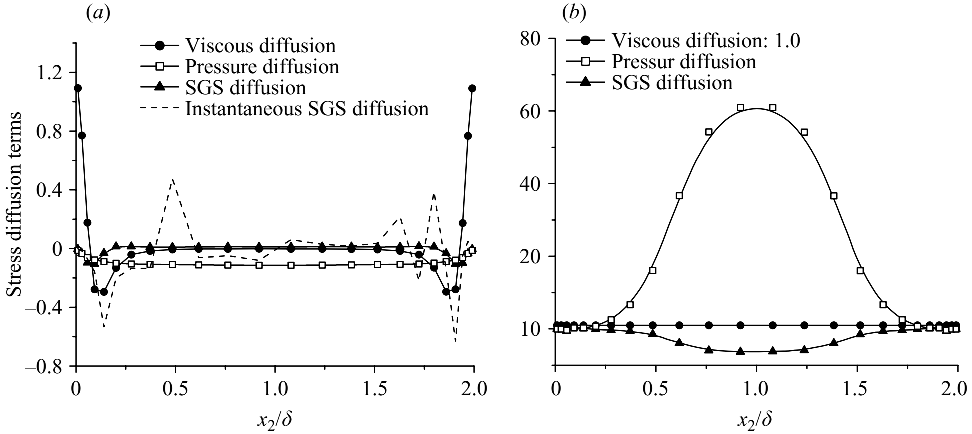

FIGURE 19. Comparison of the three k_r diffusion terms related to the stress F_{ij} (SGS stress model: DNM; SGS HF model: LGGM; $Gr = 1.3 \times 10^6$; grid resolution: $32 \times 24 \times 32$). Time- and plane-averaged values: solid lines. Instantaneous values: dashed line. Location for the instantaneous distribution of the SGS KE diffusion rate is: $x_1/L_1 = x_3/L_3 \approx 0.5$. (*a*) Non-dimensionalized using a constant wall dissipation rate $\varepsilon'_{wall} = u_\tau^4/\nu$, (*b*) non-dimensionalized using the averaged local viscous diffusion rate $\langle D_{vis} \rangle$.

figures show that the resolved viscous diffusion and dissipation terms (i.e. $\langle D_{vis} \rangle$ and $\langle \varepsilon_r \rangle$, respectively) dominate the other terms in the near-wall region, and these two terms balance each other in the vicinity of the wall (i.e. $\langle D_{vis} \rangle_{wall} = \langle \varepsilon_r \rangle_{wall}$). Note that all the quantities shown in these two figures are non-dimensionalized using a constant wall dissipation rate defined as $\varepsilon'_{wall} \overset{\text{def}}{=} u_\tau^4/\nu \approx 2\nu[\langle \bar{S}_{ij} \rangle \langle \bar{S}_{ij} \rangle]_{wall}$, where the resolved friction velocity is calculated as $u_\tau = \sqrt{\nu(\partial \langle \bar{u}_1 \rangle / \partial x_2)_{wall}}$ (see Wang *et al.* (2008) for the near-wall approximation of $\langle \bar{S}_{ij} \rangle$). The time- and plane-averaged resolved viscous dissipation term shown in figure 18 is $\langle \varepsilon_r \rangle = 2\nu \langle \bar{S}_{ij} \bar{S}_{ij} \rangle$. The Cauchy–Schwartz inequality implies that $\langle \varepsilon_r \rangle_{wall} \geqslant \varepsilon'_{wall}$ holds in the numerical calculation. Therefore, it is seen in figures 18(*a*) and 18(*b*) that $\langle \varepsilon_r \rangle_{wall} / \varepsilon'_{wall} \geqslant 1$. These figures also show that the influence of buoyancy on the budget of $\langle k_r \rangle$ is small in comparison with the other terms. In the central region of the channel, the resolved pressure diffusion term is the dominant term on the right-hand side of (4.6) which is primarily balanced the resolved convection term. The local pressure diffusion rate is mainly attributed to the local mean driving force, namely the mean streamwise pressure gradient component. The SGS effects embodied in the two SGS terms (i.e. the SGS diffusion and SGS dissipation) are finite, and become stronger as the grid resolution becomes coarser. In the remainder of this Subsection, we will further analyse the magnitudes of the SGS diffusion and dissipation terms in comparison with those of the other terms in order to quantify the SGS effects on the budget of KE of the filtered flow.

Figures 19(*a*) and 19(*b*) compare the time- and plane-averaged magnitudes of the three k_r diffusion terms related to the stress F_{ij}; namely, the resolved viscous diffusion (i.e. $\langle D_{vis} \rangle$), pressure diffusion (i.e. $\langle D_{pres} \rangle$) and SGS diffusion (i.e. $\langle D_{sgs} \rangle$) terms. The results shown in these figures are based on the coarse grid resolution. In order to compare the wall-normal distribution and relative magnitude of these three stress diffusion terms in both the near-wall and central core regions, the quantities shown in figures 19(*a*) and 19(*b*) were normalized using a constant wall dissipation rate ε'_{wall} and the time- and plane-averaged local resolved viscous diffusion rate $\langle D_{vis} \rangle$, respectively.

From figure 19(*a*), it is observed that the viscous diffusion plays a dominant role in the near-wall region for $x_2/\delta \approx 0$–0.2 and 1.8–2.0 (or for $x_2^+ = 0$–30). The pressure diffusion terms dominate the central core region for $x_2/\delta \approx 0.2$–1.8 (or $x_2^+ > 30$). Also from the figure, it is observed that the instantaneous value of SGS diffusion D_{sgs} fluctuates with a large amplitude. The averaged value of $\langle D_{sgs}\rangle$ attains its maximum negative value in the buffer region with a magnitude of $\langle D_{sgs}\rangle/\varepsilon'_{wall} \approx -0.11$ at $x_2/\delta \approx 0.08$ and 1.92 (or $x_2^+ \approx 12$). Considering that the resolved viscous dissipation rate $\langle \varepsilon_r\rangle$ reaches its maximum value at the wall (which is comparable to the value of ε'_{wall}, see figure 18), the SGS effects represented by the instantaneous and averaged values of D_{sgs} (non-dimensionalized using ε'_{wall}) are significant. Figure 19(*b*) further shows that in the central core of the channel, the magnitudes of the resolved pressure diffusion and SGS diffusion terms are much larger than the viscous diffusion term (i.e. unity after being non-dimensionalized by $\langle D_{vis}\rangle$). For instance, at $x_2/\delta \approx 1$, $\langle D_{pres}\rangle/\langle D_{vis}\rangle \approx 61.0$ and $\langle D_{sgs}\rangle/\langle D_{vis}\rangle \approx -6.31$, respectively. In other words, at the central core of the channel, the absolute magnitude of the SGS diffusion term is approximately 10.3% of the resolved pressure diffusion term, the latter being the dominant term in the budget of $\langle k_r\rangle$ here.

The SGS dissipation rate P_r represents an inertial inviscid local KE flux between the resolved and unresolved (subgrid) scales. It represents the rate of KE production and functions as a source of KE for the residual SGS motions and a sink of KE for the large resolved-scale motions. The instantaneous value of P_r can be either positive or negative, representing a local forward or backward KE flux between the resolved and subgrid scales, respectively. By definition, the value of P_r directly depends on the SGS stress model, rather than the SGS HF model. In consequence, predictions of this quantity obtained from the three proposed SGS HF models, combined with the same DNM for modelling the SGS stress, are similar. In order to elucidate the physics of the local KE transfer between resolved and subgrid scales, we show in figure 20 the time- and plane-averaged value of P_r predicted using the DNM and LGGM. The forward scatter (i.e. $\langle P_r^+\rangle$) and backscatter (i.e. $\langle P_r^-\rangle$) of KE have been separated. Naturally, these two quantities must verify $\langle P_r\rangle = \langle P_r^+\rangle + \langle P_r^-\rangle$. From figure 20, it is observed that the DNM (in conjunction with the LGGM) is capable of simulating the backscatter of KE. In contrast, owing to the simplicity and limitation of the constitutive relation inherent in the DM (which requires that the principal axes of $-\tau_{ij}^*$ be aligned with those of $\bar{S}_{ij}$), none of the combinations of the SGS models based on the DM (not shown) can successfully predict the net effect of backscatter in a time- and plane-averaged sense. This is consistent with the previous observations of Wang & Bergstrom (2005) and Wang et al (2006*a*) based on an LES study of turbulent Couette channel flows.

The SGS KE dissipation rates shown in figure 20 are normalized by the constant resolved viscous wall dissipation rate $\varepsilon'_{wall} = u_\tau^4/\nu$, which is useful for demonstrating the general wall-normal distribution pattern of the SGS dissipation rates. However, because the resolved viscous wall dissipation rate reaches its maximum value at the wall with a very large magnitude (see figure 18), the value of the SGS KE dissipation rate (after being non-dimensionalized by ε'_{wall}) is typically very small. For instance, as shown in figure 20, the level of non-dimensionalized forwardscatter is approximately 0.014 for the fine grid system and 0.041 for the coarse grid system (not shown) at the peak location (for the case of $Gr = 1.3 \times 10^6$ based on the combination of the DNM and LGGM).

In order to clearly demonstrate the relative strength of the SGS KE dissipation rate in the central core of the channel, it is beneficial to normalize its value using the local

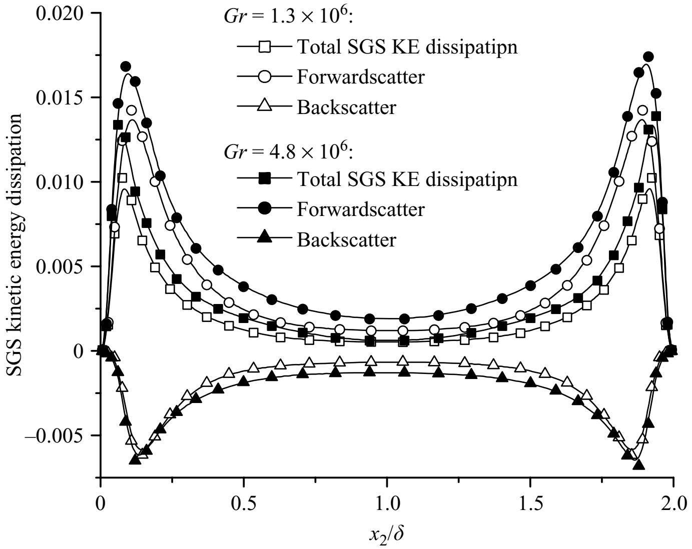

FIGURE 20. Time- and plane-averaged SGS KE dissipation rates for different Grashof numbers (SGS stress model: DNM; SGS HF model: LGGM; $Gr = 1.3 \times 10^6$; grid resolution: $48 \times 32 \times 48$). Non-dimensionalized using a constant wall dissipation rate $\varepsilon'_{wall} = u_\tau^4/\nu$. Total SGS KE dissipation: $\langle P_r\rangle/\varepsilon'_{wall}$; forwardscatter: $\langle P_r^+\rangle/\varepsilon'_{wall}$; backscatter: $\langle P_r^-\rangle/\varepsilon'_{wall}$.

viscous dissipation rate. Furthermore, the ratio between the SGS and resolved viscous dissipation rates (i.e. $\sigma_0 \overset{\text{def}}{=} P_r/\varepsilon_r$ and $\sigma \overset{\text{def}}{=} \langle P_r\rangle/\langle\varepsilon_r\rangle$) has a special physical meaning. In the context of the conventional SGS eddy viscosity (Smagorinsky) modelling approach (see §2.1), this ratio can be simplified to $\sigma_0 = \nu_{sgs}/\nu$. For a general non-eddy-viscosity SGS stress model (e.g. the DNM), the concept of SGS eddy viscosity is not directly applicable; however, in the context of time- and plane-averaging, we can define the averaged effective SGS eddy viscosity as follows: $\nu_{sgs}^e \overset{\text{def}}{=} \langle P_r\rangle/\langle 2\bar{S}_{ij}\bar{S}_{ij}\rangle = \langle P_r\rangle/\langle|\bar{\boldsymbol{S}}|^2\rangle$. As such, for the DNM, $\sigma = \langle P_r\rangle/\langle\varepsilon_r\rangle = \nu_{sgs}^e/\nu$. From figure 21, it is observed that the value of the effective SGS-to-molecular viscosity ratio σ is sensitive to the grid resolution. As the grid resolution becomes coarser, the SGS effects become, of course, more significant. For the coarse grid resolution case shown in the figure, the maximum value of σ is approximately 0.45. The levels of the forward and backward scatter of SGS KE are significant, with maximum values of $\sigma^+ \overset{\text{def}}{=} \langle P_r^+\rangle/\langle\varepsilon_r\rangle = 1.46$ and $\sigma^- \overset{\text{def}}{=} \langle P_r^-\rangle/\langle\varepsilon_r\rangle = -1.06$, respectively.

In order to evaluate the importance of the SGS effects, it is useful to compare our results for σ shown in figure 21 with those reported in the literature. It should be indicated that because the test cases used in this and those reported studies are different, the comparison to be made here should be interpreted in a qualitative, rather than quantitative, sense. In their LES study of a turbulent channel flow ($Re_\tau = 180$), Armenio & Sarkar (2002) found that the maximum value of σ is approximately 0.14 for the stably stratified case and 0.17 for the neutrally stratified case. In order to characterize the degree of the 'SGS activity' in their *a priori* and *a posteriori* LES study of a mixing layer flow, Geurts & Fröhlich (2002) introduced the parameter

$$s \overset{\text{def}}{=} \frac{\langle P_r\rangle}{\langle P_r\rangle + \langle\varepsilon_r\rangle} = \frac{\sigma}{\sigma + 1}. \tag{4.7}$$

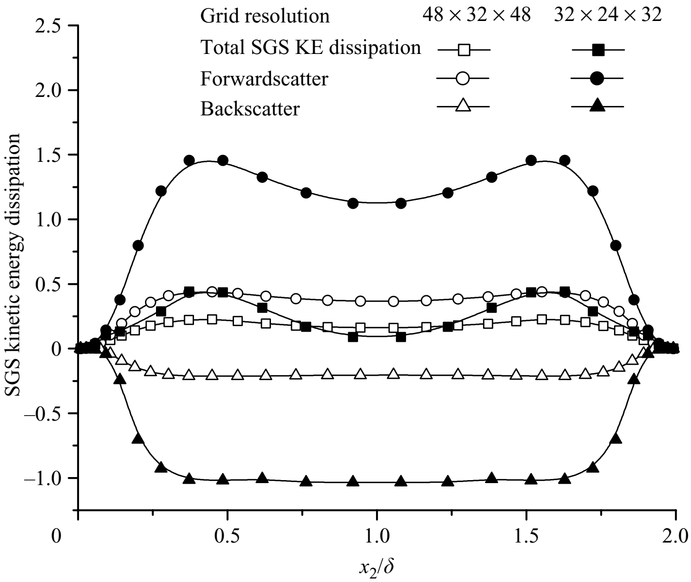

FIGURE 21. Effects of grid resolution on the SGS KE dissipation rate (SGS stress model: DNM; SGS HF model: LGGM; $Gr = 1.3 \times 10^6$). Non-dimensionalized using the time- and plane-averaged resolved viscous dissipation rate $\langle\varepsilon_r\rangle = \langle 2\nu\bar{S}_{ij}\bar{S}_{ij}\rangle$. Total SGS KE dissipation: $\langle P_r\rangle/\langle\varepsilon_r\rangle$; forwardscatter: $\langle P_r^+\rangle/\langle\varepsilon_r\rangle$; backscatter: $\langle P_r^-\rangle/\langle\varepsilon_r\rangle$.

Using this parameter, Broglia, Pascarelli & Piomelli (2003) studied SGS activity of free-surface duct flows and reported that the values of s (based on volume averaging) were approximately 0.18, 0.19, and 0.21 for $Re_\tau = 360$, 600 and 1000, which correspond to $\sigma = 0.22$, 0.23 and 0.27, respectively. Owing to the coarseness of the grid systems used in our simulations, the SGS effects shown in figure 21 are significant and generally comparable to those reported in the literature mentioned above. From this figure, it is seen that the maximum value of s is 0.31 (corresponding to $\sigma = 0.45$). Furthermore, according to the study of Geurts & Fröhlich (2002) of a temporal mixing layer flow, for a coarse grid LES, when $s < 0.5$ ($\sigma < 1$), the SGS modelling and numerical discretization errors in the LES prediction of the resolved TKE are less than 1% of the comparable quantity extracted using filtered DNS data.

4.3.2. *SGS effects on the scalar energy dissipation*

In order to further understand the role of a SGS HF model in the scalar transport, we now focus on discussing the transfer of local resolved 'scalar energy' $\bar{\theta}^2$ between the resolved and subgrid scales. Following Jiménez, Valiño & Dopazo (2001), the equation that governs the transport of the SE at the resolved scale can be derived from (2.3) as

$$\underbrace{\frac{\partial\bar{\theta}^2}{\partial t}}_{\substack{\text{transient}\\\text{term}}} + \underbrace{\frac{\partial}{\partial x_j}(\bar{u}_j\bar{\theta}^2)}_{\substack{\text{large-scale}\\\text{convection}}} = \underbrace{\alpha\frac{\partial^2\bar{\theta}^2}{\partial x_j\partial x_j}}_{\substack{\text{molecular}\\\text{diffusion}}} \underbrace{-2\alpha\frac{\partial\bar{\theta}}{\partial x_j}\frac{\partial\bar{\theta}}{\partial x_j}}_{\substack{\text{molecular}\\\text{dissipation}}} \underbrace{-2\frac{\partial}{\partial x_j}(\bar{\theta}h_j)}_{\substack{\text{SGS}\\\text{diffusion}}} + \underbrace{2h_j\frac{\partial\bar{\theta}}{\partial x_j}}_{\substack{\text{SGS}\\\text{dissipation}}}. \qquad (4.8)$$

In this equation, the non-negative definite term

$$\Gamma \overset{\text{def}}{=} 2\alpha\frac{\partial\bar{\theta}}{\partial x_j}\frac{\partial\bar{\theta}}{\partial x_j},$$

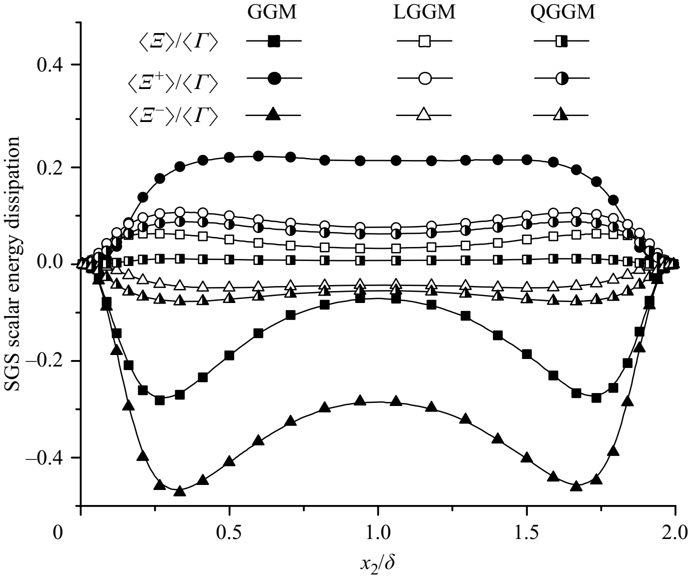

FIGURE 22. Time- and plane-averaged SGS SE dissipation rates predicted using different SGS HF models at the fine grid resolution: $48 \times 32 \times 48$ (SGS stress model: DNM; $Gr = 1.3 \times 10^6$). Total: $\langle \Xi \rangle / \langle \Gamma \rangle$; forwardscatter: $\langle \Xi^+ \rangle / \langle \Gamma \rangle$; backscatter: $\langle \Xi^- \rangle / \langle \Gamma \rangle$.

represents the resolved molecular dissipation rate which acts as a sink for the resolved scalar energy. The term

$$\Xi \overset{\text{def}}{=} -2h_j \frac{\partial \bar{\theta}}{\partial x_j}, \tag{4.9}$$

represents the local SE dissipation rate, whose value can be either positive or negative (following the usual convention, a negative sign is included in the above definition). If the value of Ξ is positive, it acts as a sink in the resolved SE transport equation (cf. (4.8)), but as a source in the transport equation of the ‘residual scalar energy’ (or ‘scalar variance’ defined as $\overline{\theta^2} - \bar{\theta}^2$) at the subgrid scale (see Jiménez *et al.* 2001 for the description of this transport equation). We refer to this case as ‘forwardscatter’ of SE flux. In contrast, if the value of Ξ is negative, it functions as a source in the resolved SE transport equation (cf. (4.8)) transferring SE from the subgrid to resolved scales, and we refer to this case as ‘backscatter’ of SE flux.

Figure 22 compares the time- and plane-averaged profiles of the local SE flux between the resolved and subgrid scales predicted using the three proposed SGS HF models (in conjunction with the SGS stress model DNM). As in the previous analysis of the local KE fluxes, the forwardscatter (i.e. Ξ^+) and backscatter (i.e. Ξ^-) of the local SE have been separated, with $\Xi = \Xi^+ + \Xi^-$. The value of $\langle \Xi \rangle$ shown in the figure is non-dimensionalized using the resolved molecular dissipation rate $\langle \Gamma \rangle$. This non-dimensionalization (i.e. $r_0 \overset{\text{def}}{=} \Xi/\Gamma$ and $r \overset{\text{def}}{=} \langle \Xi \rangle / \langle \Gamma \rangle$) has a special physical meaning. In the conventional EDM approach, $r_0 = \alpha_{sgs}/\alpha$, which is the ratio of the SGS eddy thermal diffusivity to the molecular thermal diffusivity. However, in the context of a non-eddy-thermal-diffusivity SGS modelling approach (e.g. the GGM, LGGM and QGGM), the concept of an eddy thermal diffusivity α_{sgs} is not applicable. Instead, we can define the averaged effective SGS eddy thermal diffusivity as $\alpha^e_{sgs} \overset{\text{def}}{=} \langle \Xi \rangle / \langle 2(\partial \bar{\theta}/\partial x_j)(\partial \bar{\theta}/\partial x_j) \rangle$. So, $r = \langle \Xi \rangle / \langle \Gamma \rangle = \alpha^e_{sgs}/\alpha$.

If the average value of Ξ is negative with a magnitude much larger than Γ such that the ratio between their time- and volume-averaged values $\langle\Xi\rangle_{tv}/\langle\Gamma\rangle_{tv} < -1$, the SE transport system as represented by (4.8) can become numerically unstable due to excessive backscatter of SE. From figure 22, it is observed that in the wall-normal direction, the ratio $r = \langle\Xi\rangle/\langle\Gamma\rangle$ (based on the time- and plane-averaged Ξ and Γ) ranges from −0.28 (for the GGM) to 0.07 (for the LGGM), which is a relatively small range necessary for the SE transport process being numerically stable. A perusal of figure 22 shows that the levels of both the forward and backward scatter of SE predicted by the GGM are larger than those predicted by the LGGM and QGGM. For our particular test case, the GGM slightly overpredicts the backscatter of SE. The net SGS effect on the SE transfer between the subgrid and resolved scales corresponds to backscatter for the GGM and forwardscatter for the LGGM and QGGM. The physical features observed here are related to the mathematical property of the tensor diffusivity inherent in these SGS HF models which we now explore in greater detail.

By comparing the constitutive relations of these three proposed models, it can be seen that the mathematical properties of their tensor diffusivities (as defined by (2.17), (2.20) and (2.26), respectively) are different. The trace of the tensor thermal diffusivity for the GGM (i.e. $D^G_{jk} = C_{\theta G}\mathscr{T}\tau^*_{jk}$) is zero, which is similar to the characteristics of some of the conventional models such as the DHLTDM (i.e. $D^{HL}_{jk} = C'_{\theta G}\bar{\Delta}^2\bar{S}_{jk}$ with $\mathrm{tr}(D^{HL}_{jk}) \equiv 0$) of Peng & Davidson (2002), and the DGM ($D^{DG}_{jk} = C_\theta\bar{\Delta}^2\bar{A}_{jk}$ with $\mathrm{tr}(D^{DG}_{jk}) \equiv 0$) of Porté-Agel *et al.* (2001*a,b*) and Kang & Meneveau (2002). Because the tensor thermal diffusivities for these types of SGS HF models (namely, the GGM, DHLTDM and DGM) are trace-free, they are not positive-definite. Therefore, the value of Ξ corresponding to these types of models cannot be guaranteed to be always positive. In contrast, owing to the inclusion of the Kronecker delta, the trace of the tensor diffusivity of the conventional EDM and the proposed LGGM and QGGM (i.e. the trace of D^E_{ij}, D^L_{jk} and D^Q_{jk}, respectively) is positive if $C_\theta > 0$ (for the EDM) or if $C_{\theta p} > 0$ (for the LGGM and QGGM), negative if $C_\theta < 0$ (for the EDM) or if $C_{\theta p} < 0$ (for the LGGM and QGGM), and zero if $C_\theta = 0$ (for the EDM) or if $C_{\theta p} = 0$ (for the LGGM and QGGM). This implies that the value of Ξ derived from either the EDM, LGGM or QGGM cannot be guaranteed to be always positive owing to the inherent dynamic modelling procedure (the sign of the model coefficient is dynamically determined, rather than enforced *a priori*). In summary, owing to the mathematical properties of the tensor thermal diffusivities implicit in the three proposed SGS HF models, these models are expected to be able to reflect both forward and backward scatter of local SE between the resolved and subgrid scales.

Figure 23 shows the spatial distribution of the SGS SE dissipation Ξ obtained using the LGGM and DNM based on the coarse grid system. The instantaneous and time- and plane-averaged SGS SE fluxes shown in figure 23(*a*) are non-dimensionalized using a characteristic constant molecular dissipation rate based on the wall friction velocity and temperature, namely,

$$\Gamma'_{wall} \overset{\mathrm{def}}{=} 2\theta_\tau^2 u_\tau^2/\alpha = 2\alpha\left[\frac{\partial\langle\bar{\theta}\rangle}{\partial x_2}\frac{\partial\langle\bar{\theta}\rangle}{\partial x_2}\right]_{wall}.$$

From figure 23(*a*), it is seen that the instantaneous SGS effect as indicated by the distribution of Ξ along the centreline (located at $x_1/L_1 = x_3/L_3 \approx 0.5$) is significant, with a peak value of 28% of Γ'_{wall}. As shown in the figure, the time- and plane-averaged molecular dissipation rate $\langle\Gamma\rangle$ reaches its maximum value at the wall (it

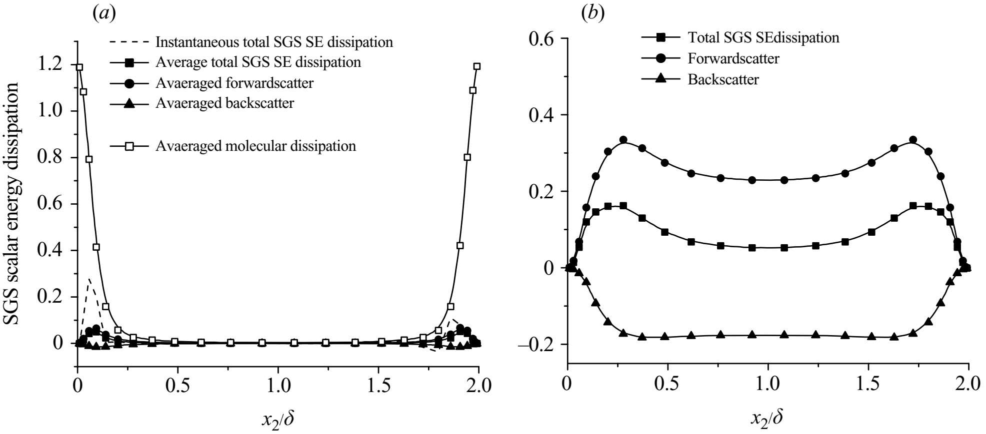

FIGURE 23. Instantaneous and time- and plane-averaged SGS SE dissipation rates at the coarse grid resolution: 32 × 24 × 32 (SGS stress model: DNM; SGS HF model: LGGM; $Gr = 1.3 \times 10^6$). Time- and plane-averaged values: solid lines. Instantaneous values: dashed line. Location for the instantaneous distribution of the SGS SE dissipation rate is: $x_1/L_1 = x_3/L_3 \approx 0.5$. (*a*) Non-dimensionalized using a constant wall dissipation rate $\Gamma'_{wall} = 2\theta_\tau^2 u_\tau^2/\alpha$, (*b*) non-dimensionalized using the averaged local viscous dissipation rate $\langle \Gamma \rangle$.

should be noted that $\Gamma'_{wall} \leqslant \langle \Gamma \rangle_{wall}$ holds necessarily owing to the Cauchy–Schwartz inequality). The pattern shown in figure 23(*a*) is dominated by the large near-wall molecular dissipation rate. Therefore, in order to clearly demonstrate the SGS effects on the SE fluxes in the central core of the channel, we show in figure 23(*b*) the SGS SE dissipation rate non-dimensionalized using the time- and plane-averaged local viscous dissipation rate $\langle \Gamma \rangle$ (which varies spatially with x_2). In comparison with figure 22, it is observed in figure 23(*b*) that as the grid resolution becomes coarser, the magnitude of the SGS SE dissipation (both forwardscatter and backscatter) becomes increasingly larger. As shown in figure 23(*b*), the maximum values for α_{sgs}^{e}/α (i.e. $\langle \Xi \rangle / \langle \Gamma \rangle$), α_{sgs}^{e+}/α (i.e. $\langle \Xi^+ \rangle / \langle \Gamma \rangle$) and α_{sgs}^{e-}/α (i.e. $\langle \Xi^- \rangle / \langle \Gamma \rangle$) are 0.17, 0.34 and –0.19, respectively. The SGS effect quantified by the value of α_{sgs}^{e}/α is comparable to that reported in Armenio & Sarkar (2002), who observed a maximum for this value of about 0.1 based on their LES study of a stably stratified turbulent channel flow ($Re_\tau = 180$). However, because the test cases used in Armenio & Sarkar (2002) and in the current study are different, this comparison of the magnitude of SGS effects should be viewed in a qualitative, rather than quantitative, sense.

5. Conclusions

The proposed QGGM derived from Noll's formula provides the most general representation of the SGS HF for the family of explicit algebraic models that are functions of the resolved temperature gradient $\partial\bar{\theta}/\partial x_j$ and SGS stress tensor τ_{ij} (i.e. $h_j = f(\tau_{ij}, \partial\bar{\theta}/\partial x_j)$). The representation of the SGS HF by the QGGM is explicit, nonlinear (quadratic), inhomogeneous, complete and irreducible. An important derivative of the QGGM is the LGGM, which is the full linear tensor thermal diffusivity SGS HF model based on $\partial\bar{\theta}/\partial x_j$ and τ_{ij}. A second important derivative of the QGGM is the GGM, which is a linear homogeneous tensor thermal diffusivity model that is analogous to the well-known GGDH approach of Daly & Harlow (1970) as applied within the RANS framework. We demonstrate that the proposed GGM, LGGM and QGGM are general linear and nonlinear SGS HF models which include as special cases a number of previous models such as the EDM of Moin *et al.* (1991), DHLTDM of Peng & Davidson (2002), and DFLTDM and DNTDM of Wang *et al.* (2007*b*).

In order to validate the proposed modelling approach, a comparative numerical study of the predictive performance of a number of SGS stress and HF models has been conducted with reference to neutrally and unstably stratified horizonal channel flows. In comparison with the DNS data, it was demonstrated that the GGM, LGGM and QGGM can successfully reproduce salient features of the resolved fluid and temperature fields including predictions of the characteristic large longitudinal vortex rolls, mean and fluctuations of the resolved velocity and temperature, budget of the shear stresses and heat fluxes, and forward and backward scattering of local kinetic and scalar energy fluxes. It is observed that in comparison with the conventional DM of Lilly (1992), use of the DNM for modelling the SGS stress improves predictions of both the velocity and temperature fields at the resolved scale.

Owing to the coarseness of the grid systems used in the present simulations, the instantaneous and averaged SGS effects are shown to be important in capturing the correct physics of the flow. When the DNM is used in conjunction with the LGGM on the coarse grid, the maximum value of the time- and plane-averaged effective SGS-to-molecular viscosity ratio (i.e. $\sigma = \langle P_r\rangle/\langle\varepsilon_r\rangle = \nu^e_{sgs}/\nu$) is approximately 0.45. The levels of the forward and backward scattered SGS KE are significant, with maximum values of $\sigma^+ = \langle P_r^+\rangle/\langle\varepsilon_r\rangle = \nu^{e+}_{sgs}/\nu = 1.46$ and $\sigma^- = \langle P_r^-\rangle/\langle\varepsilon_r\rangle = \nu^{e-}_{sgs}/\nu = -1.06$, respectively. At the central core of the channel, the magnitude of the SGS diffusion is much larger than that of the viscous diffusion, with $\langle D_{sgs}\rangle/\langle D_{vis}\rangle \approx -6.31$, indicating that the SGS motions play a significant role in the diffusion of the resolved KE $\langle k_r\rangle$ of the filtered velocity field (even in a time- and plane-averaged sense). The maximum value of the ratio of the averaged effective SGS thermal diffusivity to the molecular thermal diffusivity (i.e. $\alpha^e_{sgs}/\alpha = \langle\Xi\rangle/\langle\Gamma\rangle$) is 0.17 for the coarse grid tested. In the forward and backward scattering of the SGS SE $\bar{\theta}^2$, the maximum value of this ratio α^e_{sgs}/α can reach 0.34 and -0.19, respectively. The maximum value of the ratio of the averaged SGS shear stress to the averaged total Reynolds shear stress (i.e. $-\langle\tau_{12}\rangle/(-\langle\bar{u}_1''\bar{u}_2''\rangle - \langle\tau_{12}\rangle)$) is 7.4% and 14.9% for the fine and coarse grid systems, respectively. Taken together, these results (obtained using the DNM and LGGM) suggest that the SGS effects in the current simulations are important and need to be explicitly accounted for in order to obtain the improved prediction accuracy.

On utilization of the DNM for modelling the SGS stress, the predictive performance of the GGM, LGGM and QGGM is generally comparable for the flow simulated in this study, although it should be noted that the performance of the LGGM and QGGM is slightly better than that of GGM (in terms of the predictions of the RMS of the resolved temperature field $\bar{\theta}^+_{rms}$ and the streamwise turbulent heat flux $\langle\bar{u}_1''\bar{\theta}''\rangle^+ + \langle h_1\rangle^+$). With respect to the need for advancing the theory of constitutive relations for SGS scalar-flux modelling, the three models proposed here are important. Taken together, these three proposed SGS HF models constitute a useful generalization of the current state of the art for SGS scalar-flux modelling within the LES context.

Although the matrix system for computing the model coefficients for the QGGM requires additional numerical operations in comparison with those for the LGGM and GGM, the computational time for the simulations is still dominated by the pressure solver and the difference in computational cost is hardly noticeable between the different SGS HF modelling approaches. However, if attention is focused instead on the degree of modelling complexity, on the mathematical properties of the tensor thermal diffusivity, on the level of forward and backward scatter of SGS scalar energy, and on the general predictive performance of the numerical simulations, the LGGM appears to be more appealing than the GGM and QGGM. Although the test results here are encouraging, in order to obtain a more comprehensive understanding of the predictive accuracy of the new SGS HF models, more extensive *a priori* and *a posteriori* LES studies based on different test cases involving a greater range of Reynolds and Grashof numbers will be required in future studies.

Support from the National Sciences and Engineering Research Council (NSERC) in the form of a Visiting Fellowship to B.C.W. is gratefully acknowledged.

REFERENCES

Armenio, V. & Sarkar, S. 2002 An investigation of stably stratified turbulent channel flow using large-eddy simulation. *J. Fluid Mech.* **459**, 1–42.

Avancha, R. V. R. & Pletcher, R. H. 2002 Large eddy simulation of the turbulent flow past a backward-facing step with heat transfer and property variations. *Intl. J. Heat Fluid Flow* **23**, 601–614.

Bardina, J., Ferziger, J. H. & Reynolds, W. C. 1980 Improved Subgrid-Scale Models for Large-Eddy Simulation. *AIAA Paper* 80-1357.

Batchelor, G. K. 1949 Diffusion in a field of homogeneous turbulence. *Austral. J. Sci. Res.* A **2**, 437–450.

Broglia, R., Pascarelli, A. & Piomelli, U. 2003 Large-eddy simulations of ducts with a free surface. *J. Fluid Mech.* **484**, 223–253.

Clark, R. A., Ferziger, J. H. & Reynolds, W. C. 1979 Evaluation of subgrid-scale models using an accurately simulated turbulent flow. *J. Fluid Mech.* **91**, 1–16.

Dailey, L. D., Meng, N. & Pletcher, R. H. 2003 Large eddy simulation of constant heat flux turbulent channel flow with property variations: quasi-developed model and mean flow results. *Trans. ASME: J. Heat Transfer* **125**, 27–38.

Daly, B. J. & Harlow, F. H. 1970 Transport equations in turbulence. *Phys. Fluids* **13**, 2634–2649.

Fukui, K., Nakagima, M. & Ueda, H. 1991 Coherent structure of turbulent longitudinal vortices in unstably-stratified turbulent flow. *Intl. J. Heat Mass Transfer* **34**, 2373–2385.

Fureby, C. & Grinstein, F. F. 1999 Monotonically integrated large eddy simulation of free shear flows. *AIAA J.* **37**, 544–556.

Garg, R. P., Ferziger, J. H., Monismith, S. G. & Koseff, J. R. 2000 Stably stratified turbulent channel flows. I. Stratification regimes and turbulence suppression mechanism. *Phys. Fluids* **12**, 2569–2594.

Gatski, T. B. & Speziale, C. G. 1993 On explicit algebraic stress models for complex turbulent flows. *J. Fluid Mech.* **254**, 59–78.

Germano, M., Piomelli, U., Moin, P. & Cabot, W. H. 1991 A dynamic subgrid-scale eddy viscosity model. *Phys. Fluids* A **3**, 1760–1765.

Geurts, B. J. & Fröhlich, J. 2002 A framework for predicting accuracy limitations in large-eddy simulation. *Phys. Fluids* **14**, L41–L44.

Ghosal, S. & Rogers, M. M. 1997 A numerical study of self-similarity in a turbulent plane wake using large-eddy simulations. *Phys. Fluids* **9**, 1729–1739.

Hanjalić, K. 2002 One-point closure models for buoyancy-driven turbulent flows. *Annu. Rev. Fluid Mech.* **34**, 321–347.

Higgins, C. W., Parlange, M. B. & Meneveau, C. 2004 The heat flux and the temperature gradient in the lower atmosphere. *Geophys. Res. Lett.* **31** (L22105), 1–5.

Horiuti, K. 2003 Roles of non-aligned eigenvectors of strain-rate and subgrid-scale stress tensors in turbulence generation. *J. Fluid Mech.* **491**, 65–100.

Iida, O. & Kasagi, N. 1997 Direct numerical simulation of unstably stratified turbulent channel flow. *Trans. ASME: J. Heat Transfer* **119**, 53–61, DNS data available from the Turbulence and Heat Transfer Laboratory (N. Kasagi) at University of Tokyo, http://www.thtlab.t.u-tokyo.ac.jp/.

Jiménez, C., Valiño, L. & Dopazo, C. 2001 *A priori* and *a posteriori* tests of subgrid scale models for scalar transport. *Phys. Fluids* **13**, 2433–2436

Kang, H. S. & Meneveau, C. 2002 Universality of large eddy simulation model parameters across a turbulent wake behind a heated cylinder. *J. Turbul.* **3** (32), 1–27.

Kawamura, H. 2007 DNS Database of wall turbulence and heat transfer (dataset: Poi150_2nd_A.dat), Kawamura Laboratory at Tokyo University of Science, http://murasun.me.noda.tus.ac.jp/turbulence/.

Keating, A., Piomelli, U., Bremhorst, K. & Nešić, S. 2004 Large-eddy simulation of heat transfer downstream of a backward-facing step. *J. Turbul.* **5** (20), 1–27.

Kim, J. & Moin, P. 1985 Application of a fractional-step method to incompressible Navier-Stokes equations. *J. Comput. Phys.* **59**, 308–323.

Launder, B. E. 1988 On the computation of convective heat transfer in complex turbulent flows. *Trans. ASME: J. Heat Transfer* **110**, 1112–1128.

Lee, J. S., Xu, X. & Pletcher, R. H. 2004 Large eddy simulation of heated vertical annular pipe flow in fully developed turbulent mixed convection. *Intl. J. Heat Mass Transfer*. **47**, 437–446.

Lilly, D. K. 1992 A proposed modification of the Germano subgrid-scale closure method. *Phys. Fluids* A **4**, 633–635.

Lumley, J. L. 1970 Toward a turbulent constitutive relation. *J. Fluid Mech.* **41**, 413–434.

Moin, P., Squires, K., Cabot, W. & Lee, S. 1991 A dynamic subgrid-scale model for compressible turbulence and scalar transport. *Phys. Fluids* A **3**, 2746–2757.

Pallares, J. & Davidson, L. 2002 Large-eddy simulations of turbulent heat transfer in stationary and rotating square ducts. *Phys. Fluids* **14**, 2804–2816.

Park, T. S., Sung, H. J. & Suzuki, K. 2003 Developemnt of a nonlinear near-wall turbulence model for turbulent flow and hear transfer. *Intl. J. Heat Fluid Flow* **24**, 29–40.

Peng, S.-H. & Davidson, L. 2002 On a subgrid-scale heat flux model for large eddy simulation of turbulent thermal flow. *Intl. J. Heat Mass Transfer* **45**, 1393–1405.

Pope, S. B. 1975 A more general effective-viscosity hypothesis. *J. Fluid Mech.* **72**, 331–340.

Pope, S. B. 2000 *Turbulent Flows.* Cambridge University Press.

Porté-Agel, F., Pahlow, M., Meneveau, C. & Parlange, M. B. 2001*a* Atmospheric stability effect on subgrid-scale physics for large-eddy simulation. *Adv. Water Resour.* **24**, 1085–1102.

Porté-Agel, F., Parlange, M. B., Meneveau, C. & Eichinger, W. E. 2001*b* *A priori* field study of the subgrid-scale heat fluxes and dissipation in the atmospheric surface layer. *J. Atmos. Sci.* **58**, 2673–2698.

Pullin, D. I. 2000 A vortex-based model for the subgrid flux of a passive scalar. *Phys. Fluids* **12**, 2311–2319.

Reiner, M. 1945 A mathematical theory of dilatancy. *Am. J. Maths.* **67**, 350–362.

Rhie, C. M. & Chow, W. L. 1983 Numerical study of the turbulent flow past an isolated airfoil with trailing edge separation. *AIAA J.* **21**, 1525–1532.

Rivlin, R. S. 1948 Large elastic deformations of isotropic materials. iv. further developments of the general theory. *Phil. Trans. R. Soc. Lond.* A **241**, 379–397.

Rodi, W. 1976 A new algebraic relation for calculating the Reynolds stresses. *Z. Angew. Math. Mech.* **56**, T219–T221.

Rogers, M. M., Mansour, N. N. & Reynolds, W. C. 1989 An algebraic model for the turbulent flux of a passive scalar. *J. Fluid Mech.* **203**, 77–101.

Sagaut, P. 2002 *Large Eddy Simulation for Incompressible Flows: An Introduction*, 2nd edn. Springer.

Salvetti, M. V. & Banerjee, S. 1995 *A priori* tests of a new dynamic subgrid-scale model for finite-difference large-eddy simulations. *Phys. Fluids* **7**, 2831–2847.

So, R. M. C., Jin, L. H. & Gatski, T. B. 2004 An explicit algebraic Reynolds stress and heat flux model for incompressible turbulence: Part II bouyant flow. *Theor. Comput. Fluid Dyn.* **17**, 377–406.

So, R. M. C. & Speziale, C. G. 1999 A review of turbulent heat transfer modeling. In *Annual Review of Heat Transfer* (ed. C. L. Tien), vol. 10, chap. 5, pp. 177–219. Begell House.

Spencer, A. J. M. 1971 Part III: Theory of invariants. In *Continuum Physics, Volume I–Mathematics* (ed. A. C. Eringen). Academic.

Speziale, C. G. 1987 On nonlinear k–l and k–ϵ models of turbulence. *J. Fluid Mech.* **178**, 459–475.

SUGA, K. & ABE, K. 2000 Nonlinear eddy viscosity modelling for turbulence and heat transfer near wall and shear-free boundaries. *Intl. J. Heat Fluid Flow* **21**, 37–48.

STOLZ, S., ADAMS, N. A. & KLEISER, L. 2001 The approximate deconvolution model for large-eddy simulations of compressible flows and its application to shock-turbulent-boundary-layer interaction. *Phys. Fluids* **13**, 2985–3001.

TYAGI, M. & ACHARYA, S. 2005 Large eddy simulations of flow and heat transfer in rotating ribbed duct flows. *Trans. ASME: J. Heat Transfer*. **127**, 486–498.

VREMAN, A. W. 2004 An eddy-viscosity subgrid-scale model for turbulent shear flows: Algebraic theory and applications. *Phys. Fluids* **16**, 3670–3681.

WANG, B.-C. & BERGSTROM, D. J. 2005 A dynamic nonlinear subgrid-scale stress model. *Phys. Fluids* **17**, 035109, 1–15.

WANG, B.-C., BERGSTROM, D. J., YIN, J. & YEE, E. 2006*a* Turbulence topologies predicted using large eddy simulations. *J. Turbul.* **7** (34), 1–28.

WANG, B.-C., YEE, E. & BERGSTROM, D. J. 2006*b* Geometrical description of the subgrid-scale stress tensor based on Euler axis/angle. *AIAA J.* **44**, 1106–1110.

WANG, B.-C., YEE, E., YIN, J. & BERGSTROM, D. J. 2007*a* A general dynamic linear tensor-diffusivity subgrid-scale heat-flux model for large-eddy simulation of turbulent thermal flows. *Numer. Heat Transfer*. B **51**, 205–227.

WANG, B.-C., YIN, J., YEE, E. & BERGSTROM, D. J. 2007*b* A complete and irreducible dynamic SGS heat-flux modelling based on the strain rate tensor for large-eddy simulation of thermal convection. *Intl. J. Heat Fluid Flow* **28**, 1227–1243.

WANG, B.-C., YEE, E. & BERGSTROM, D. J. 2008 Geometrical properties of the vorticity vector derived using large-eddy simulation. *Fluid Dyn. Res.* **40**, 123–154.

WANG, L. & LU, X.-Y. 2004 An investigation of turbulent oscillatory heat transfer in channel flows by large eddy simulation. *Intl. J. Heat Mass Trans.* **47**, 2161–2172.

WIKSTRÖM, P. M., WALLIN, S. & JOHANSSON, A. V. 2000 Derivation and investigation of a new explicit algebraic model for the passive scalar flux. *Phys. Fluids* **12**, 688–702.

WINCKELMANS, G. S., JEANMART, H. & CARATI, D. 2002 On the comparison of turbulence intensities from large-eddy simulation with those from experiment or direct numerical simulation. *Phys. Fluids* **14**, 1809–1811.

YOSHIZAWA, A. 1988 Statistical modelling of passive-scalar diffusion in turbulent shear flows. *J. Fluid Mech.* **195**, 541–555.

YOUNIS, B. A., SPEZIALE, C. G. & CLARK, T. T. 2005 A rational model for the turbulent scalar fluxes. *Proc. R. Soc. Lond.* A **461**, 575–594.

ZHENG, Q.-S. 1994 Theory of representations for tensor functions—a unified invariant approach to constitutive equations. *Appl. Mech. Rev.* **47**, 545–587.